

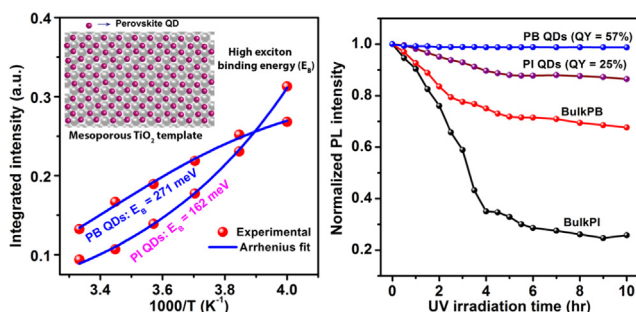
## Regular Article

# Large exciton binding energy, high photoluminescence quantum yield and improved photostability of organo-metal halide hybrid perovskite quantum dots grown on a mesoporous titanium dioxide template

Sumaiya Parveen<sup>a</sup>, Kamal Kumar Paul<sup>a</sup>, Ruma Das<sup>a</sup>, P.K. Giri<sup>a,b,\*</sup><sup>a</sup> Department of Physics, Indian Institute of Technology Guwahati, Guwahati 781039, India<sup>b</sup> Centre for Nanotechnology, Indian Institute of Technology Guwahati, Guwahati 781039, India

## GRAPHICAL ABSTRACT

Fluorine-doped mesoporous-TiO<sub>2</sub>-template-grown ultra-small organo-metal halide hybrid perovskite quantum dots exhibiting large exciton binding energy, high photoluminescence quantum yield and improved photostability.



## ARTICLE INFO

## Article history:

Received 8 October 2018

Revised 2 December 2018

Accepted 29 December 2018

Available online 31 December 2018

## Keywords:

Perovskite nanoparticles  
Mesoporous F-TiO<sub>2</sub>  
Strong quantum confinement  
Photoluminescence quantum yield  
Temperature dependent photoluminescence  
High exciton binding energy  
Stability

## ABSTRACT

Herein, we demonstrated a novel synthetic route to grow size-tunable hybrid perovskite (CH<sub>3</sub>NH<sub>3</sub>PbI<sub>3</sub> and CH<sub>3</sub>NH<sub>3</sub>PbBr<sub>3</sub>) quantum dots (QDs) using a Fluorine-doped TiO<sub>2</sub> (F-TiO<sub>2</sub>) mesoporous template and these QDs exhibit large exciton binding energy, high photoluminescence quantum yield and improved photostability. The pore size in F-TiO<sub>2</sub> template is tuned by varying the HF molar concentration during its solvothermal growth and size of the perovskite QDs embedded in F-TiO<sub>2</sub> pores is tuned in the range 1.7–5.1 nm, as revealed from the TEM analysis. A systematic blue-shift in UV–visible absorption edge, as well as photoluminescence (PL) spectrum, is observed with the reduced size of the perovskite QDs due to strong quantum confinement. The CH<sub>3</sub>NH<sub>3</sub>PbI<sub>3</sub> QD with average size ~1.7 nm exhibits ~47 nm blue shift in the PL spectra, ~43 fold enhancement in PL intensity and ~25% PL quantum yield (QY). On the other hand, CH<sub>3</sub>NH<sub>3</sub>PbBr<sub>3</sub> QD of similar size exhibits dramatically enhanced (~124 times) PL emission with narrow line width and a PLQY of ~57%, which is significant for the template-assisted growth of perovskite QDs film. The quantitative analysis of the PL emission energy vs QD size shows an excellent fit with the Brus equation confirming the strong quantum confinement effect in the perovskite QDs. Analysis of low-temperature PL spectra reveals very high exciton binding energy (162–272 meV) for the QDs as compared to the bulk film (32 meV) due to the high effective dielectric constant, and high electron-hole recombination probability in the QDs, which is consistent with the extremely high PLQY and stable emission from the QDs. The blue shift of the PL peak with increasing

\* Corresponding author at: Department of Physics, Indian Institute of Technology Guwahati, Guwahati 781039, India.

E-mail address: [giri@iitg.ernet.in](mailto:giri@iitg.ernet.in) (P.K. Giri).

temperature is explained on the basis of localization effect. Time-resolved PL analysis for both the perovskite QDs reveals faster life time compared to their bulk counterparts, confirming the significant radiative recombination of carriers in the QDs at the room temperature. The  $\text{CH}_3\text{NH}_3\text{PbBr}_3$  QDs embedded in porous F-TiO<sub>2</sub> template maintain its initial PL intensity up to several hours ( $\geq 10$  h) under the UV laser exposure (18mW), while that of the bulk film decreases to <67%. Thus, template grown hybrid perovskite QDs exhibiting high photostability and very high PLQY demonstrated here are promising for the next generation optoelectronic applications.

© 2018 Elsevier Inc. All rights reserved.

## 1. Introduction

Organic-inorganic halide perovskites have fostered unprecedented research interest due to their rapidly achieved spectacular performance in the field of optoelectronic devices along with their remarkable characteristics, such as low cost, long-range charge transport, tunable optical band gap, high absorption coefficient and photoluminescence quantum yield (PLQY) [1–9]. Currently, perovskite-based solar cells have achieved power conversion efficiency up to 22% and LEDs have achieved quantum efficiency as high as 10% [10]. Additionally, other applications of perovskite, such as sensors, amplified spontaneous emission and lasing, photodetectors, memory devices have also been realized.

In recent years, perovskite nanocrystals (NCs) have drawn great attention owing to their unique properties, such as large exciton binding energy, narrow emission bandwidth, high PLQY, decent stability along with the well-known properties of bulk perovskite [11–18]. Lead bromide based perovskite quantum dots (QDs) in colloidal solution have approached  $\sim 100\%$  PLQY, synthesized by colloidal method [19]. Schmidt and co-workers first demonstrated the synthesis of  $\sim 6$  nm sized organic-inorganic halide perovskite NCs through a simple method using ammonium bromide with a medium-length alkyl chain [20]. Since then, perovskite NCs are being prepared by different methods for a wide range of optoelectronic applications. In the case of NCs synthesized by the colloidal method, the final product consists of NCs with some unwanted bulk structures. The as-synthesized colloidal perovskite NCs are ionic and essentially hygroscopic in nature, which makes them usually unstable in the ambient environment [21–24]. Perovskite solution may be incorporated in various mesoporous templates, confining the growth of perovskite in the pores, which results in the controlled growth of perovskite NCs guided by the mesoporous structure. Researchers have devoted great efforts to synthesize different templates, since in-situ fabrication process of perovskite NCs is preferable for device applications. Kojima et al. observed strong photoluminescence (PL) emission from nanocrystalline lead bromide perovskite synthesized by rapid self-organization on a mesoporous aluminum oxide film [25]. Di et al. demonstrated the formation of self-assembled perovskite NCs embedded in a solid organic matrix [26]. Malgras et al. described a simple method to grow monodisperse 3.3 nm sized  $\text{CH}_3\text{NH}_3\text{PbBr}_{x-3}$  NCs inside mesoporous silica templates by varying the pore size of the templates [27]. Recently, Anaya et al. reported tunable quantum confinement (QC) effect over a wide range of 0.34 eV by embedding the perovskite NCs in thin metal oxide films [28]. Though the size-tunable perovskite nanoparticles (NPs) are successfully achieved in the earlier works, very few studies discuss on the improvement of fluorescence intensity and their application in light-emitting devices. Demchyshyn et al. used nanoporous anodic alumina (npAAO) and silicon (npSi) thin films for the growth of perovskite nanocrystals with very high PLQY (up to 25% for  $\text{CH}_3\text{NH}_3\text{PbI}_3$ , 60% for  $\text{CH}_3\text{NH}_3\text{PbBr}_3$ , 90% for  $\text{CsPbBr}_3$ ) and they also demonstrated blue emission from  $\text{CsPbBr}_3$  in npSi and cyan EL in npAAO-based LEDs [29]. Recently, Ghosh et al. reported growth

of  $\text{CH}_3\text{NH}_3\text{PbI}_3$  NPs on a mesoporous Si nanowire template and they achieved  $\sim 12$  fold enhancement in PL intensity with respect to bulk perovskite film and a PLQY of  $\sim 9\%$  [30]. The reported PLQY of template grown perovskite NCs is typically quite low and needs further improvement for device applications.

Herein, we demonstrate the growth of  $\text{CH}_3\text{NH}_3\text{PbI}_3$  and  $\text{CH}_3\text{NH}_3\text{PbBr}_3$  QDs inside a mesoporous Fluorine doped TiO<sub>2</sub> (F-TiO<sub>2</sub>) template by a simple solution processed method. The perovskite QDs are uniformly grown on the pores of the F-TiO<sub>2</sub> template and the size of the perovskite QD is consistent with the pore size of F-TiO<sub>2</sub> template, as evidenced from field emission scanning electron microscope (FESEM) and transmission electron microscope (TEM) analyses. The ultra-small perovskite QDs exhibit remarkably high band gap, intense PL emission and high PLQY due to the strong QC effect. Low-temperature PL analysis exhibits very high exciton binding energy of perovskite QDs consistent with the enhanced and stable PL emission of QDs. Time-resolved PL (TRPL) studies reveal faster decay time for the QDs, confirming the dominance of radiative recombination of charge carriers in QDs, thus revealing the mechanism behind high PLQY from perovskite QDs. These template grown perovskite QDs also exhibit much better photostability and air stability compared to bulk films, which is very promising for its practical application including the light emitting diodes.

## 2. Experimental procedure

### 2.1. Materials

The starting materials for the present work are Ti foil (99.7%, Sigma Aldrich), hydrofluoric acid (48%, Merck), hydrochloric acid (37%, Merck), methylamine solution ( $\text{CH}_3\text{NH}_3$ , 33 wt% in absolute ethanol, Sigma-Aldrich), lead(II) iodide ( $\text{PbI}_2$ , 99%, Sigma-Aldrich), lead(II) bromide ( $\text{PbBr}_2$ , 99.999%, Sigma-Aldrich), hydroiodic acid (HI, 57 wt% in water, Sigma-Aldrich), hydrobromic acid (HBr, 48 wt% in water, Sigma-Aldrich), N,N-dimethylformamide (DMF, >99%, Sigma-Aldrich), diethyl ether (>99%, Merck), Titania paste, transparent (Sigma-Aldrich).

### 2.2. Synthesis procedures

#### 2.2.1. Synthesis of porous TiO<sub>2</sub> nanostructures

Mesoporous 3D F-TiO<sub>2</sub> nanoflowers (NFs) with self-grown TiO<sub>2</sub> NCs were prepared using the procedure reported by Paul et al. [31]. In a typical synthesis, commercially available Ti foil was first cleaned by 18% aqueous HCl solution at 90 °C for 20 min to remove impurities and oxide layers. Afterward, it was rinsed with DI water vigorously and finally dried in the inert gas atmosphere. Cleaned Ti foil was taken into a Teflon-lined autoclave (Berghof, BR-100) with 50 mL of aqueous HF solution (20–80 mM). The sealed autoclave was heated and maintained at 150 °C for 8 h. After the hydrothermal treatment, the autoclave was allowed to cool down naturally and then the foil was gently washed with

DI water and dried in an oven at 90 °C to get the mesoporous F-TiO<sub>2</sub> templates. The mesoporous F-TiO<sub>2</sub> templates grown with 20 mM, 40 mM, and 80 mM HF concentrations are named as F1, F2 and F3, respectively.

### 2.2.2. Synthesis of CH<sub>3</sub>NH<sub>3</sub>PbI<sub>3</sub>

CH<sub>3</sub>NH<sub>3</sub>PbI<sub>3</sub> perovskite precursor solution was prepared using the well-established procedure [32]. To prepare CH<sub>3</sub>NH<sub>3</sub>I powder, 24 mL of methylamine solution was diluted with 50 mL of absolute ethanol and stirred for 15 min in 250 mL round-bottom flask. Then, 8 mL of hydroiodic acid was slowly added to the above solution at 0 °C with vigorous stirring at 1000 rpm for 2 h. Afterward, the solution was heated at 60 °C for 5 h with continuous stirring to evaporate the solvent. To remove impurities from the obtained white CH<sub>3</sub>NH<sub>3</sub>I powder, the crystals were washed several times with anhydrous diethyl ether and dried at 60 °C in a vacuum oven overnight. Then, CH<sub>3</sub>NH<sub>3</sub>I and PbI<sub>2</sub> were dissolved in DMF at 1:1 M ratio to obtain the semi-transparent yellow CH<sub>3</sub>NH<sub>3</sub>PbI<sub>3</sub> perovskite solution with 30 wt%.

### 2.2.3. Synthesis of CH<sub>3</sub>NH<sub>3</sub>PbBr<sub>3</sub>

We followed a similar procedure to obtain the CH<sub>3</sub>NH<sub>3</sub>PbBr<sub>3</sub> perovskite precursor solution. CH<sub>3</sub>NH<sub>3</sub>Br was first prepared by adding 8 mL methylamine and 2.83 mL hydrobromic acid solution to 22 mL of absolute ethanol. For the elimination of impurities and recrystallization of CH<sub>3</sub>NH<sub>3</sub>Br, the same procedure has been followed, as discussed for the synthesis of CH<sub>3</sub>NH<sub>3</sub>I powder. The as-prepared CH<sub>3</sub>NH<sub>3</sub>Br powder was dissolved together with PbBr<sub>2</sub> at a 2:1 M ratio in DMF, to get a transparent colorless CH<sub>3</sub>NH<sub>3</sub>PbBr<sub>3</sub> solution with a concentration of 30 wt%.

### 2.2.4. Growth of perovskite QDs on F-TiO<sub>2</sub>

The synthesis of CH<sub>3</sub>NH<sub>3</sub>PbI<sub>3</sub> and CH<sub>3</sub>NH<sub>3</sub>PbBr<sub>3</sub> QDs was carried out by spin coating the as-synthesized perovskite solution on the F-TiO<sub>2</sub> template at 2500 rpm for 30 sec, followed by annealing at 80 °C for 20 min. The perovskite coated templates F1, F2, and F3 are named as F1PI, F2PI and F3PI for CH<sub>3</sub>NH<sub>3</sub>PbI<sub>3</sub>, respectively, and F1PB, F2PB and F3PB for CH<sub>3</sub>NH<sub>3</sub>PbBr<sub>3</sub>, respectively. Fig. 1 illustrates the schematic of the template-assisted growth process of perovskite QDs. To compare the performance of perovskite QDs grown on F-TiO<sub>2</sub>, commercially available mesoporous TiO<sub>2</sub> paste (m-TiO<sub>2</sub>) was also used as a template to grow perovskite film/NPs. For this, commercial m-TiO<sub>2</sub> paste was first diluted in ethanol and then spin coated on ITO substrate and subsequently PI and PB solutions were deposited m-TiO<sub>2</sub> layer. Note that the m-TiO<sub>2</sub> contains pores of much larger size than that of the mesoporous F-TiO<sub>2</sub>, as discussed later.

## 2.3. Characterization techniques

Several microscopic and spectroscopic tools have been utilized to study the morphology, structure and optical properties of different samples. The details of the characterization techniques including absolute PL quantum yield measurement have been provided in the Supporting Information, Section S1.

## 3. Results and discussion

### 3.1. Morphology studies

Surface morphology of as-synthesized F-TiO<sub>2</sub> template with arbitrary shaped TiO<sub>2</sub> NCs was investigated by FESEM and the low magnification images are shown in Fig. S1 (a–c) (Supporting information). These images clearly reveal the nanoflowers (NF) type morphology of the F-TiO<sub>2</sub> nanostructures. Fig. 2 portrays the surface morphology of pristine F-TiO<sub>2</sub> NF template. It is evident from Fig. 2(a) that for sample F1 (grown with 20 mM HF), the self-grown TiO<sub>2</sub> NCs are observed to be uniformly decorated on the NF surface, due to the irregular surface etching by HF during the hydrothermal treatment. Histogram showing the separation between two consecutive NCs in F1 is depicted in Fig. S1(d) (Supporting Information) with an average separation of 3.2 nm. The inter-particle gap serves as pore-like structure and acts as the template for the growth of perovskite QDs. When the HF concentration increases from 20 mM to 40 mM, surface etching is more prominent and thus the size of the NCs is observed to be increased, as shown in Fig. 2(b). As a result of the intense surface etching, separation between consecutive NCs increases and it is estimated to be 4.8 nm for F2, as shown in Fig. S1(e) (Supporting Information). For 80 mM HF concentration, the inter-particle separation is further increased, as shown in Fig. 2(c). In this case, the average inter-particle separation is 6.4 nm (F3), as shown in Fig. S1(f) (Supporting Information). In the course of spin coating of perovskite solution on the F-TiO<sub>2</sub> template, the PI or PB QDs are formed in the inter-particle gaps (voids/pores) of TiO<sub>2</sub> NCs. After the decoration of perovskite QDs, the inter-particle gap/voids in F-TiO<sub>2</sub> templates are observed to be filled, as shown in Fig. S2(a–c) (Supporting Information), resulting in the uniform decoration of perovskite QDs in the pores of F-TiO<sub>2</sub> template. Due to the resolution limit of FESEM imaging, perovskite QDs are not clearly discernable here. However, the size of perovskite QDs increases from F1PI to F3PI, which is consistent with the pore size in the mesoporous F-TiO<sub>2</sub> NF template. To compare the performance of perovskite QDs grown on F-TiO<sub>2</sub>, commercially procured mesoporous TiO<sub>2</sub> paste (m-TiO<sub>2</sub>) was also used as a template to grow perovskite NPs. Fig. S3 (Supporting Information) shows FESEM image of PI and PB deposited on m-TiO<sub>2</sub> coated substrates revealing bulk nature

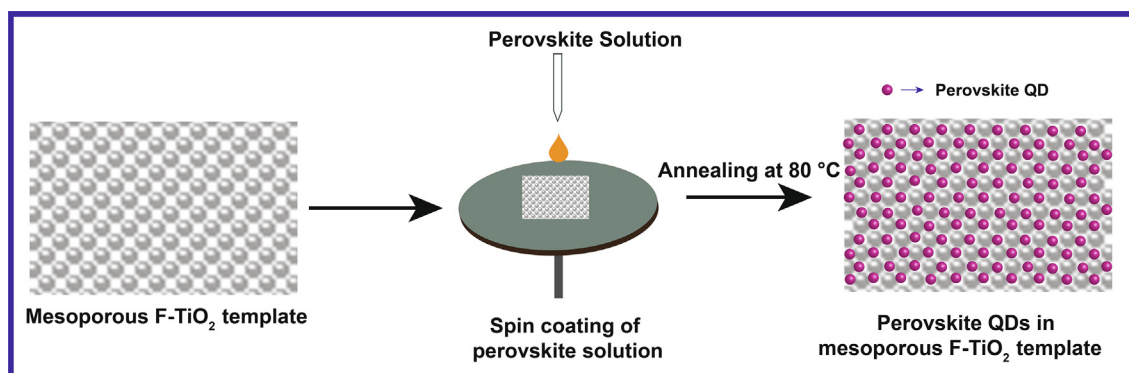
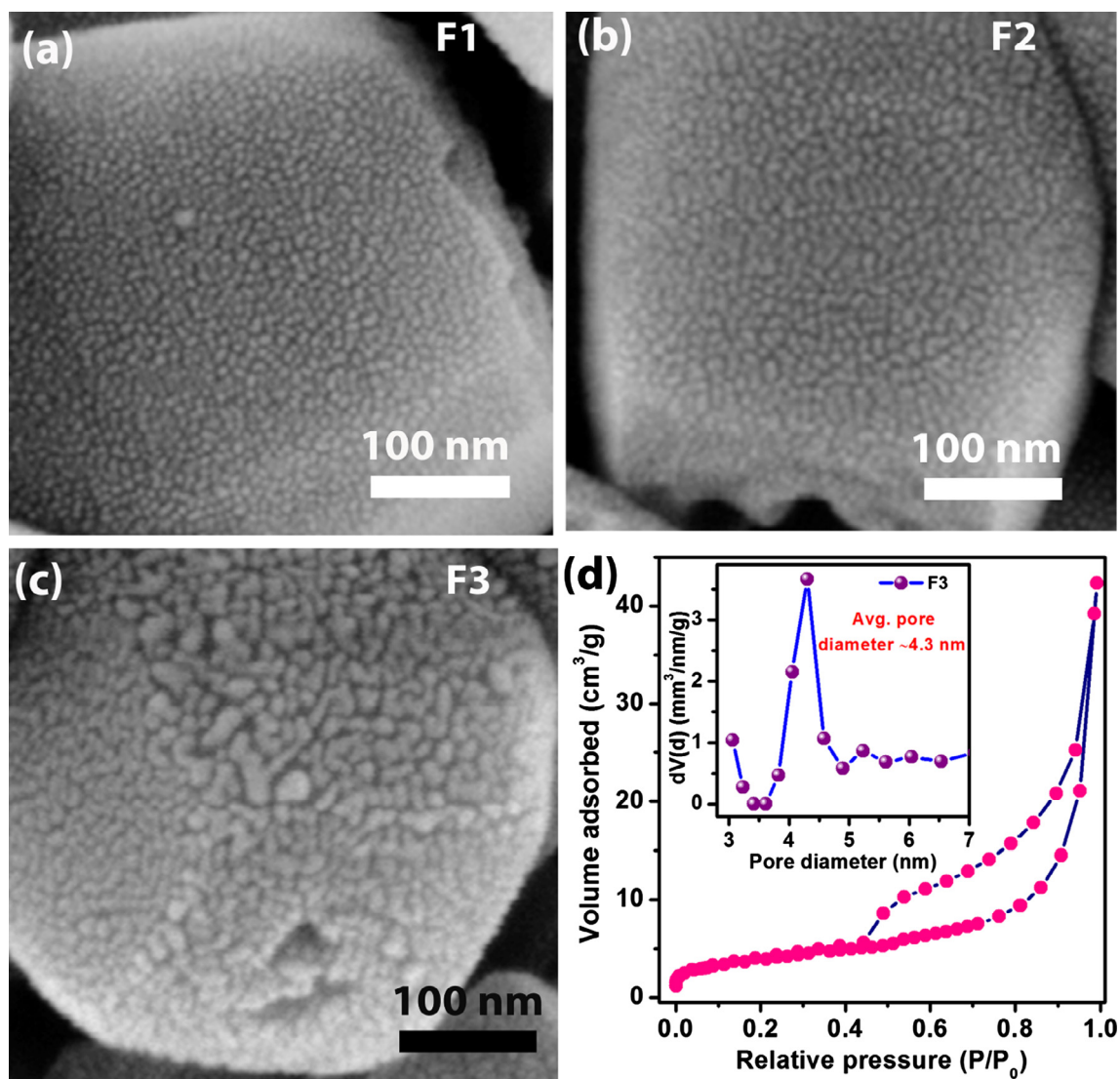


Fig. 1. Schematic of hydrothermally grown mesoporous F-TiO<sub>2</sub> template and growth of perovskite QDs on it by spin coating followed by annealing.



**Fig. 2.** FESEM images of mesoporous F-TiO<sub>2</sub> petals grown at different HF concentrations: (a) 20 mM (F1), (b) 40 mM (F2) and (c) 80 mM (F3). (d) N<sub>2</sub> adsorption/desorption isotherms of F-TiO<sub>2</sub> NF template obtained from F3. The inset shows the corresponding BJH pore size distribution.

of the perovskite, since the pore sizes in m-TiO<sub>2</sub> is very large (>30 nm). Energy dispersive X-ray (EDX) spectrum of the as-synthesized F-TiO<sub>2</sub> NF (F1) is shown in Fig. S4 (Supporting Information) confirming the presence of Ti, O, and F in the NF. The concentration of F is observed to be ≈8 at% with HF concentration 20 mM, which confirms the doping and surface adsorption of fluorine ion on F-TiO<sub>2</sub> NF surface [31]. In contrast, commercially procured m-TiO<sub>2</sub> paste does not have any fluorine doping (see Fig. S4(b), Supporting Information) and hence intrinsic in nature and it behaves differently for the light emission characteristic of the perovskite layer on it.

The surface area and pore size of the as-grown F-TiO<sub>2</sub> NF template as well as commercially available mesoporous m-TiO<sub>2</sub> paste were measured by the Brunauer–Emmett–Teller (BET) process. The N<sub>2</sub> adsorption-desorption isotherms of F3 are shown in Fig. 2 (d) and the isotherms of F-TiO<sub>2</sub> NF exhibit an abrupt increase in the high-pressure region (>0.7P/P<sub>0</sub> value), which can be related to the capillary condensation and multilayer adsorption of N<sub>2</sub> in the voids between F-TiO<sub>2</sub> NCs. The average pore size and corresponding size distribution was analyzed using Barrett-Joyner-Halenda (BJH) analysis. The BJH pore size distribution profile for F3 is shown in the inset of Fig. 2(d). The mean surface area and

average pore diameter of F3 are measured to be 13.836 m<sup>2</sup>/g and 4.3 nm, respectively. Note that the pore diameter calculated from BET is less than the estimated inter-particle separation between TiO<sub>2</sub> NCs from FESEM image, which is primarily due to the resolution limit of the FESEM. The N<sub>2</sub> adsorption-desorption isotherms and the BJH pore size distribution profiles for commercially available mesoporous m-TiO<sub>2</sub> paste are shown in Fig. S5(a and b) (Supporting Information). The average pore diameter of m-TiO<sub>2</sub> is ~32.9 nm, which is too large to grow perovskite QDs using it as a template.

TEM images of the PI QDs grown on F-TiO<sub>2</sub> templates were acquired to investigate the actual size and morphology of individual QD. To prepare the TEM sample, F-TiO<sub>2</sub> layer with the PI QDs was scratched from the Ti foil (substrate) in the form of powder and then dispersed in toluene. Next, the dispersion was drop casted on the TEM grid and heated at ~45 °C to evaporate the solvent. Fig. 3(a) shows the TEM image of the sample F1PI revealing the uniform decoration of PI QDs on the F-TiO<sub>2</sub> template. The corresponding size distribution of PI QDs with average size 1.7 nm is shown in the inset of Fig. 3(a). Fig. 3(b) shows the bright field high-resolution STEM image of F1PI discerning the discrete distribution of PI QDs on F-TiO<sub>2</sub> template. The uniform growth of PI QDs

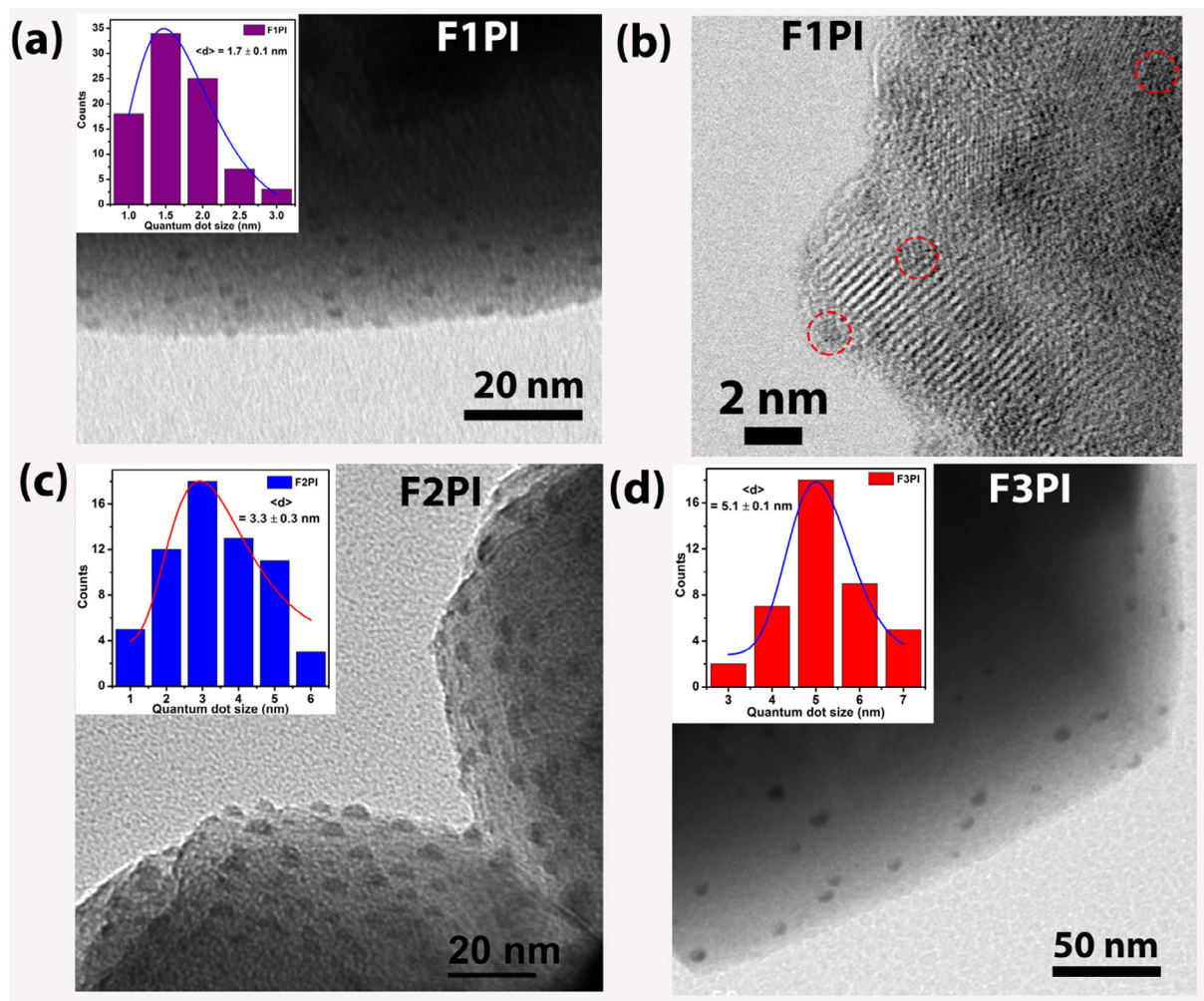


**Fig. 3.** (a) TEM image of PI QDs in F1PI and corresponding size distribution in the inset. (b) High resolution bright field STEM image of F1PI. TEM image of PI QDs in: (c) F2PI and (d) F3PI and the corresponding size distributions shown in the insets.

on the F-TiO<sub>2</sub> templates of F2 and F3 are shown in Fig. 3(c) and (d), and the corresponding particle size distribution with an average diameter of 3.3 nm and 5.1 nm are shown in the insets, respectively. Since the size of the QDs grown on F1 is smaller than that of F2 and F3, it facilitates stronger QC effect, which will be discussed later. It is evident from the TEM images that the size of the as-grown PI QDs on F-TiO<sub>2</sub> template becomes larger with the increase of the molar concentration of HF. The estimated size of the PI QDs from the TEM images is consistent with the average pore size or interparticle separation between F-TiO<sub>2</sub> NCs in different samples. We find that the average size of the QDs in F3PI is  $\sim 5.1$  nm, which is marginally higher than the pore diameter of F3 ( $\sim 4.3$  nm) calculated using BJH analysis. Hence, the perovskite QDs are partially embedded in the pores of the F-TiO<sub>2</sub> template and partially outside the pores, which is fully consistent with the TEM images. Thus, the TEM results reveal that the ultra-small pores in the F-TiO<sub>2</sub> template act as nucleation sites for the growth of perovskite QDs. After spin coating and annealing of the perovskite solution, PI QDs start to crystallize and exhibits superior properties. High-angle annular dark field (HAADF) image of the elemental mapping for F1PI is shown in Fig. S6(a) (Supporting Information). The elemental mapping clearly shows the presence of C, N, Pb and I on F-TiO<sub>2</sub> template confirming the presence of PI QDs on F-TiO<sub>2</sub> template. To compare the properties of QDs grown on F-TiO<sub>2</sub> template with that grown by colloidal method,

we prepared colloidal QDs following the method reported by Huang et al. [33] and samples are termed as cPI and cPB corresponding to PI and PB precursors, respectively. cPI and cPB QDs with average QD size  $\sim 2$  nm were successfully synthesized, as shown in Fig. S7(a and b) (Supporting Information), and utilized for the comparison of light emission properties along with stability.

### 3.2. Structural analysis

#### 3.2.1. XRD study

In order to confirm the crystal structure and phase of the bulk perovskite films and PI/PB QDs, XRD pattern of each sample has been recorded and shown in Fig. S8(a) (Supporting Information). Each characteristic diffraction peak of crystalline PI matches with the literature [34,35]. No trace of the PbI<sub>2</sub> peak ( $2\theta = 12^\circ$ ) is observed, which confirms the complete transformation of precursor materials (CH<sub>3</sub>NH<sub>3</sub>I and PbI<sub>2</sub>) into PI. As evident from the XRD pattern, both the PI QDs and the F-TiO<sub>2</sub> template are highly crystalline in nature and the F-TiO<sub>2</sub> template is observed to be mostly in anatase phase (marked as “A” in the figure) with a small trace of brookite phase (marked as “B”). Fig. 4(a) shows the XRD pattern corresponding to (1 1 0) plane of PI QDs grown within the voids of F-TiO<sub>2</sub> template along with the bulk PI film grown on the ITO substrate. Characteristic diffraction peak intensity for

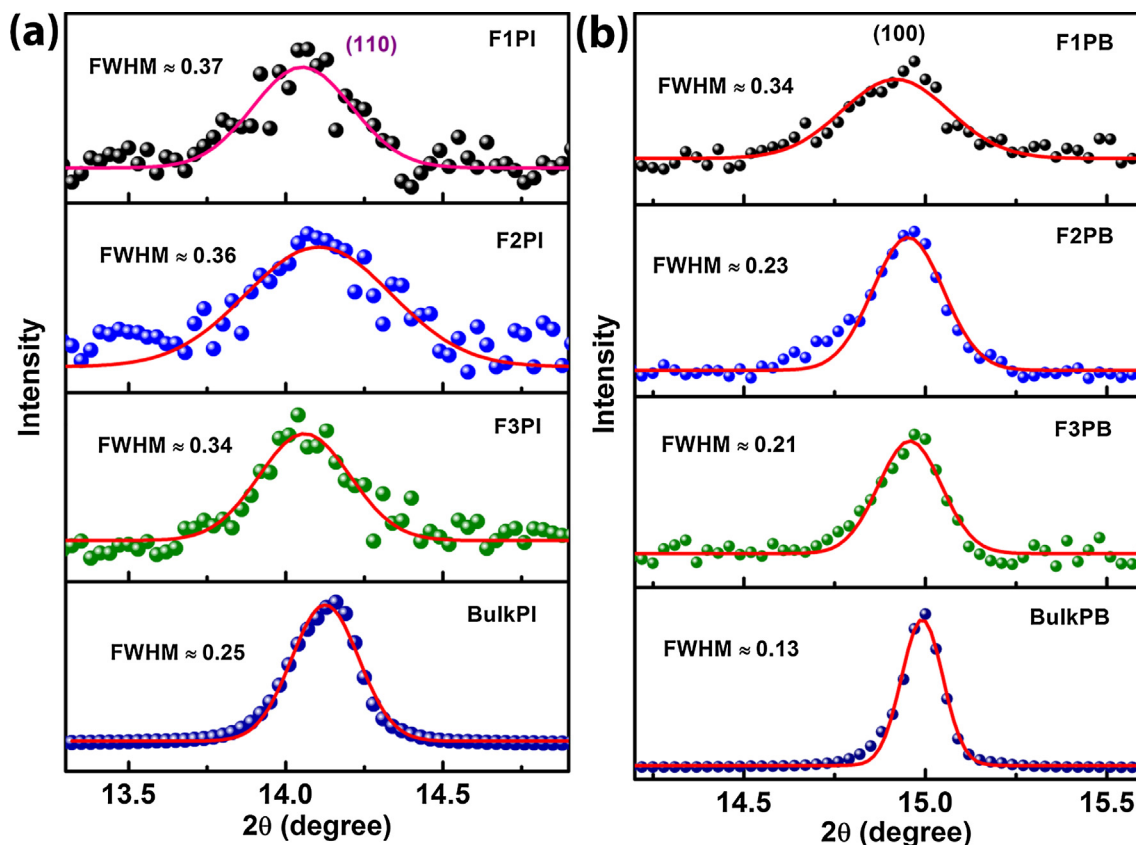


Fig. 4. A comparison of XRD pattern of different perovskite QDs: (a) (1 1 0) diffraction peak for PI QDs and (b) (1 0 0) diffraction peak for PB QDs, grown on various F-TiO<sub>2</sub> templates.

(1 1 0) plane of PI QDs decreases as compared to BulkPI film, which may be due to the lower thickness/volume of PI QDs. With decreasing size of PI QDs, the XRD peak is observed to be broadened systematically, as evident from Fig. 4(a). The (1 1 0) peak position slightly shifts to lower angle as the size of the PI QDs decreases which indicates the presence of tensile strain due to the formation of QDs. The full width at half maximum (FWHM) of (1 1 0) peak for smallest PI QDs (F1PI) is estimated to be  $\sim 0.37^\circ$ , which is  $\sim 1.5$  times than that of the BulkPI. Thus, the increase in FWHM is consistent with the formation of ultra-small size QDs. Though the Scherrer formula can predict the crystallite size of PI QDs grown on various F-TiO<sub>2</sub> templates, finer estimation of the QD size is difficult due to the low intensity of the diffraction peak. In this case, Scherrer formula gives a higher estimate of the size of the QDs as compared to that measured from TEM, primarily due to their ultra-small sizes where the validity of the formula is questionable. Fig. S8(b) (Supporting Information) shows the XRD patterns of BulkPB and PB QDs grown on F-TiO<sub>2</sub> templates, suggesting the highly crystalline cubic phase of PB crystals. Fig. 4(b) shows the XRD pattern corresponding to (1 0 0) plane of PB NPs grown on various F-TiO<sub>2</sub> templates along with the bulk PB film. Similar to the PI NPs, the (1 0 0) plane shifts to lower angle and the line width for F1PB increases systematically with decreasing the NP size and the FWHM is estimated to be  $\sim 2.6$  times higher than that of the BulkPB case. The possibility of ultra-thin capping layer of perovskite film on the F-TiO<sub>2</sub> NF is unlikely, since the XRD intensity is low and line width is relatively large for the QDs. To confirm the same, ultra-thin ( $\sim 4$  nm) PB film was deposited on ITO substrate by vapor deposition method and it showed  $\sim 3$  times stronger XRD peak intensity compared to that of the QD case (Fig. S9, Supporting Information). In the presence of any additional poly-

crystalline layer of perovskite film on the surface of the F-TiO<sub>2</sub>, the intensity of XRD pattern would be more intense, which is contrary to our observation. Hence, the presence of any capping layer seems to be unlikely in the present case.

### 3.3. Optical analysis

#### 3.3.1. UV-Vis absorption studies

Diffuse reflectance spectra (DRS) of the as-grown samples are studied to understand the change in the band structure due to the formation of perovskite NPs. From the DRS, Kubelka-Munk (K-M) function,  $F(R)$  is calculated which is related to the absorption coefficient ( $\alpha$ ) given by,

$$F(R) = \frac{(1 - R)^2}{2R} = \frac{\alpha}{S} \quad (1)$$

where  $R$  is the diffuse reflectance,  $S$  is the scattering coefficient. Fig. 5(a) exhibits the plot of the K-M function for PI QDs on various F-TiO<sub>2</sub> templates and from the figure, a significant blue shift (up to 51 nm for F1PI) in the absorption edge of the PI QDs is observed with respect to that of the BulkPI film on ITO substrate, which is clearly noticeable from the magnified view of the plot for F1PI and BulkPI shown in inset of Fig. 5(a). Among different PI samples, the absorption edge of F1PI is observed maximally blue shifted, which may be due to the strong QC effect in the PI QDs in F1PI, since it contains the smallest size QDs. As the size of the QDs decreases below the exciton Bohr radius, there is a sharp transition in the absorption band due to excitonic transition [36]. For comparison, cPI QDs dispersed in toluene was spin coated on ITO coated glass substrate to measure the absorption spectra. Fig. S10(a) (Supporting

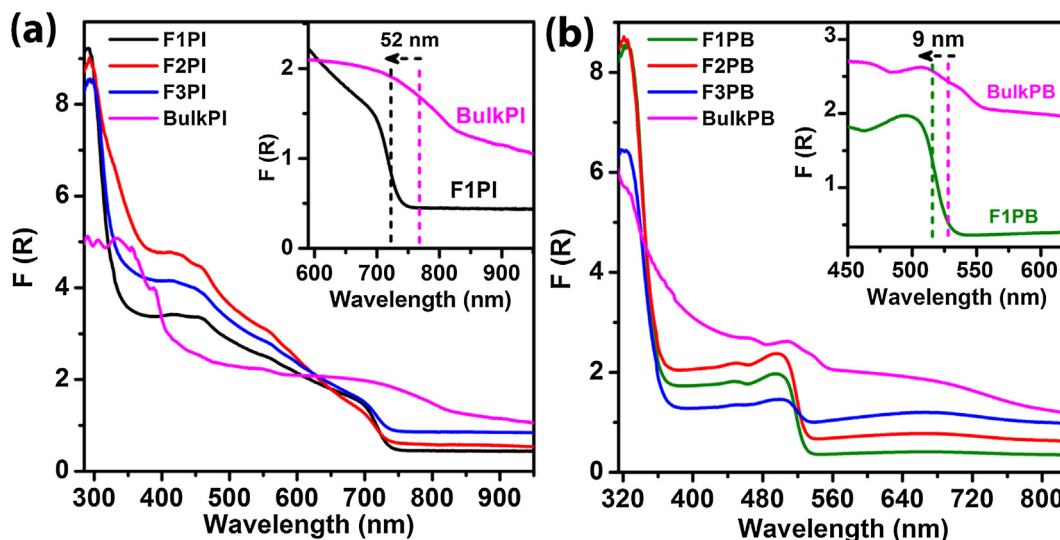


**Fig. 5.** (a) A plot of Kubelka-Munk function,  $F(R)$ , for PI QDs grown on the different mesoporous F-TiO<sub>2</sub> template and the BulkPI film deposited on ITO substrate (BulkPI). The inset shows an enlarged view of absorption edge for F1PI and BulkPI indicating the blue shift of the absorption edge in F1PI with respect to the BulkPI film. (b) A comparison of the Kubelka-Munk functions for the samples F1PB, F2PB, F3PB and BulkPB film. The inset shows the blue shift of the absorption edge in F1PB as compared to that of BulkPB. (For interpretation of the references to color in this figure legend, the reader is referred to the web version of this article.)

**Information**) shows absorbance of cPI QDs synthesized using a top down approach with absorbance band edge at  $\sim 711$  nm.

To compare the optical properties of PB NPs grown in a similar way,  $F(R)$  for different samples was analyzed. Fig. 5(b) shows a comparison of  $F(R)$  of the sample F1PB, F2PB, F3PB, and BulkPB film. Though, a similar blue shift is observed for PB QDs compared to its bulk counterpart, PB QDs exhibit much lesser blue shift than PI QDs. In both the cases, the absorption spectra of perovskite QDs exhibit clear band edge step indicating its direct band gap nature and the  $F(R)$  of bulk films is observed to be higher than the perovskite QDs, may be because of the higher thickness of bulk perovskite film than the QDs. The contribution of F-TiO<sub>2</sub> absorption is observed at  $\sim 350$  nm with a sharp edge and at a higher wavelength (beyond 400 nm) it possesses negligible absorbance [37,38]. Thus, the absorbance corresponding to the perovskite QDs observed in the visible region has a negligible contribution from the F-TiO<sub>2</sub> template. Absorbance data of cPB QDs are shown in Fig. S10(b) (Supporting Information), which shows an absorption edge of  $\sim 520$  nm.

### 3.3.2. Photoluminescence studies

Due to the ultra-small size of the QDs, QC effect is expected to be prominent in PL spectrum, since quantization of energy levels and enlargement of the band gap are the most prominent consequences of confinement in semiconductor QDs. PL spectra for the PI QDs were recorded using a 405 nm laser excitation in ambient condition. Fig. 6(a) shows a comparison of PL spectra for pristine F1, BulkPI and F1PI. Note that pristine F1 does not show any measurable PL intensity in the visible region for the 405 nm excitation, while the BulkPI film possesses a relatively sharp PL peak centered at 762 nm, due to the direct band to band transition. The PI QDs grown on F1 template shows dramatically high PL intensity as compared to that of the bare F1 and BulkPI. Fig. 6(b) exhibits comparative PL spectra of PI QDs grown over the various F-TiO<sub>2</sub> templates with different pore size under identical conditions of measurement. PL intensity of PI QDs is observed to be remarkably increased when the size of the QDs decreased, as depicted in the inset of Fig. 6(b). As compared to the BulkPI film, the PL intensities of F1PI, F2PI, and F3PI are observed to be enhanced by  $\sim 41$ , 22 and 19 times, respectively, due to the reduced size of the QDs. A

normalized spectra corresponding to Fig. 6(b) is displayed in Fig. 6(c) showing a systematic blue shift in PL peak position from F3PI to F1PI with the decrease in the size of the PI QDs, which is fully consistent with the absorption spectra. This strongly indicates the QC effect in the perovskite QDs confined in the pores of mesoporous F-TiO<sub>2</sub> templates. PI QDs grown within the mesoporous F-TiO<sub>2</sub> template display sharp PL peaks at 716 nm (F1PI), 721 nm (F2PI) and 737 nm (F3PI), which are observed to be blue-shifted from that of BulkPI (764 nm). The PL spectrum for F1PI is maximally blue shifted (47 nm) with respect to the BulkPI film. This gradual shift of PL peak towards the higher energy is an indication of enlargement of the optical band gap due to the quantum size effect [27]. Each PL spectrum for PI QDs possesses relatively broader line width (FWHM  $\sim 86$  nm) as compared to the BulkPI film ( $\sim 47$  nm), which may be associated with the size distribution of PI QDs on the F-TiO<sub>2</sub> template. Additionally, Förster energy transfer process from smaller to the larger QDs is reported to be prominent for the large size distribution of QDs. Thus, the higher energy emission from the smaller QDs may contribute to the overall broadening of the PL emission [39].

In order to quantify the quantum size effect of PB based perovskite QDs, comparative PL spectra were recorded for the PB QDs using a 355 nm laser excitation in ambient condition. Fig. 6(d) shows a comparison of PL spectra for the pristine F1, BulkPB film and PB QDs grown on F1, which depicts dramatically enhanced PL intensity from F1PB compared to both the pristine F1 and BulkPB film. Fig. 6(e) shows a comparison of PL spectra of PB QDs grown on different F-TiO<sub>2</sub> templates and BulkPB film. As evident from the inset of Fig. 6(e), the PL emission from F1PB is exceptionally intense and estimated to be  $\sim 124$  fold higher than that of the BulkPB film. The corresponding normalized PL spectra are shown in Fig. 6(f), which reveals a small blue shift ( $\sim 10$  nm) for the smallest size PB QDs (F1PB) as compared to the BulkPB film. FWHM of PL spectra for F1PB, F2PB, and F3PB are observed to be 24 nm, 28 nm and 26 nm, respectively, while that for the BulkPB film is estimated to be 31 nm. Thus, the reduction in line width of PL spectra for the PB QDs indicates its high color purity in emission, which is promising for the fabrication of efficient green LEDs. Note that the F-TiO<sub>2</sub> NFs template possesses very low oxygen vacancy defects and thus minor absorption in the visible-NIR

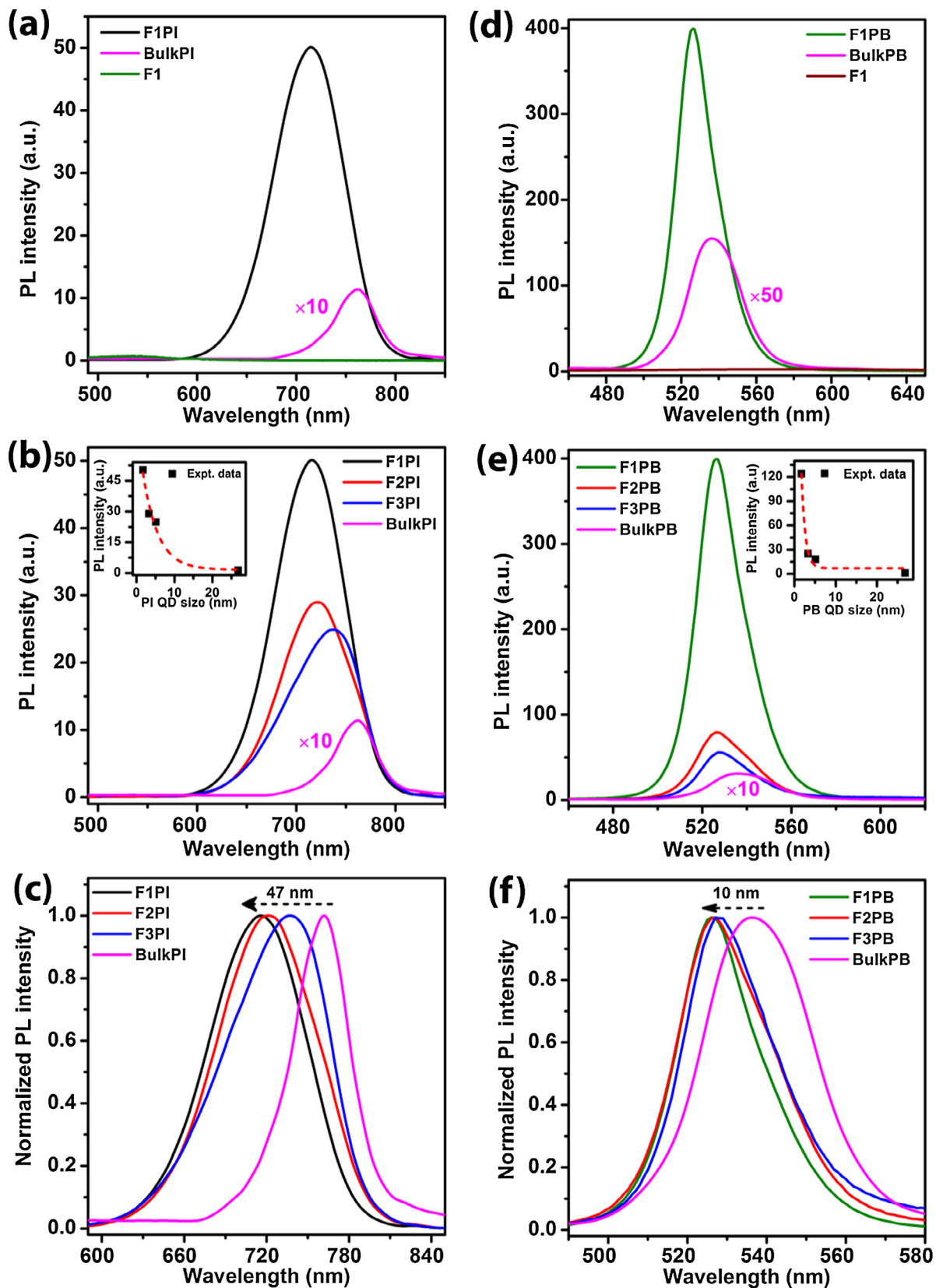


**Fig. 6.** (a) A comparison of PL spectra of pristine F1, BulkPI and F1PI, (b) comparison of PL spectra of F1PI, F2PI, F3PI and BulkPI film and inset is showing variation of PL intensity with PI QD size, (c) the corresponding normalized PL spectra showing the blue shift of the PL peak up to 47 nm, (d) Comparison of PL spectra of pristine F1, BulkPB and F1PB, (e) comparison of PL spectra of various PB QDs with BulkPB, while inset shows the variation of PL intensity with PB QD size and (f) the corresponding normalized PL spectra. To enable comparison of intensities, some of the spectra are multiplied by the factors mentioned in respective image. (For interpretation of the references to color in this figure legend, the reader is referred to the web version of this article.)

region. Since the absorption intensity of the F-TiO<sub>2</sub> template in the visible-NIR region is extremely low, the emission from the perovskite QDs is minimally affected by the reabsorption.

Emission properties of PI and PB QDs grown on F-TiO<sub>2</sub> templates are compared with perovskite QDs synthesized using the top down method. PL emission of cPI QDs is found to be centered at ~721 nm (see Fig. S11(a) Supporting Information). PL intensity of F1PI is ~20 times higher than that of the cPI QD film, for similar concentration. Fig. S11(b) (Supporting Information) shows the PL spectrum of cPB QDs with excitonic emission centered at ~525 nm and FWHM ~ 31 nm. Though cPB QDs show slightly higher (~1.2 times) PL intensity than the F1PB, the line width of PL spectrum is higher for cPB QDs than that of PB QDs grown on F-TiO<sub>2</sub> template indicating high color purity of perovskite QDs grown in case of F1PB. Again, for comparison, PL spectra of PI and PB film deposited on m-TiO<sub>2</sub> are compared with BulkPI and BulkPB film (see Fig. S12, Supporting Information). For both the cases, the PL emission is less for m-TiO<sub>2</sub> template, which may be due to the well-known electron accepting nature of the m-TiO<sub>2</sub> layer [40]. In the present case, F-TiO<sub>2</sub> template is Fluorine doped (as confirmed from EDX) and Fluorine acts as *n*-type donor in TiO<sub>2</sub>, which increases its electron concentration and reduces the probability of electron transfer from perovskite layer causing high recombination. Seo et al. reported that Fluorine passivates the oxygen vacancy defects and acts as an extrinsic *n*-type donor for F-TiO<sub>2</sub> by increasing the concentration of free electrons in the conduction band of F-TiO<sub>2</sub> [41]. This also leads to increase in surface electron concentration and enhanced catalytic activity by electron spill-over effect [42]. In our case, since the F-TiO<sub>2</sub> layer is electron rich, it minimizes the possibility of electron injection from the perovskite QDs to the F-TiO<sub>2</sub> layer. Using XPS analysis, it was reported that hydrothermally grown F-TiO<sub>2</sub> NCs contain two major peaks related to physical adsorption of F ions on the surface of the F-TiO<sub>2</sub> flowers and substitution of F atoms in the F-TiO<sub>2</sub> lattice [31]. This leads to the electron rich F-TiO<sub>2</sub> layer in the present case and strongly enhanced PL emission, compared to the commercial m-TiO<sub>2</sub> case.

A quantitative analysis of the blue shift with QD size and the origin of the lower blue shift in PB QDs than the PI QDs are investigated using the well-known Brus equation [43]. Due to larger dielectric constant of PI than that of PB, the blue shift in PL is larger for PI than that of PB. More details of the explanation are presented in Section S2 (supporting information).

A summary of room temperature PL features with the size distribution of perovskite QDs is shown in Tables 1 and 2. Fig. 7(a) shows the variations of PLQY for the samples PI QDs and BulkPI, while Fig. 7(b) shows the comparison of PLQY for PB QDs along with BulkPB. The PLQY of PI and PB QDs grown on the F1 template are measured to be 25% and 57%, respectively, which are significantly high compared to the bulk film as well as the other reported works in template-assisted growth of perovskite NPs [27,28,30]. High PLQY of perovskite QDs indicates low non-radiative recombination of excitons in QDs. Note that higher QY reported for the PB QDs is usually obtained with colloidal QDs solution, while the present results correspond to QD film on F-TiO<sub>2</sub> substrate/template. Hence, the observed high PLQY is considered to be significant for the development of QD thin film based LEDs etc. The increase in

**Table 2**Details of the PL characteristics of the CH<sub>3</sub>NH<sub>3</sub>PbBr<sub>3</sub> (PB) QDs.

Sample	Peak position (nm)	Intensity enhancement factor	PLQY (%)
F1PB	526	124	57
F2PB	527	25	13
F3PB	528	18	11
BulkPB	536	1	5

PL intensity and high PLQY in case of perovskite QDs may be due to the high exciton binding energy, which prevents the dissociation of excitons prior to radiative decay, increasing the emission probability [44]. The excitons in bulk perovskite with binding energy 28–75 meV are reported to be 3D Wannier type, which facilitates strong delocalization as it is close to the thermal energy at room temperature (RT) (~26 meV), tending to dissociate into free carriers before recombining radiatively, which results in low PLQY in bulk film [20,32,45,46]. In contrast, the QDs or NCs possess sufficiently high exciton binding energy (~100 meV), which prevents their easy dissociation at RT, resulting in the enhanced PL emission. Additionally, efficient radiative recombination of photogenerated charge carriers and passivation of nonradiative recombination may be one of the boosting factors for the high PLQY of perovskite QDs, which is further confirmed from the TRPL analysis (discussed later). F1PI sample contains uniformly decorated ultra-small size PI QDs (~1.7 nm), facilitating the extraordinary enhancement in PL emission. It is reported that the exciton Bohr radius ( $R_B$ ) of CH<sub>3</sub>NH<sub>3</sub>PbI<sub>3</sub> is ~3 nm and thus to realize the strong QC, the condition  $d/R_B < 2$  should be obeyed [28,47–49]. In the present case, the size of the QDs for all the samples satisfies the above condition to exhibit the strong confinement effect.

In order to analyze further the QC effect quantitatively, the dependence of the size of the PI QDs on their PL properties has been analyzed. Fig. 7(c) shows a plot of PL peak energy vs the size of the corresponding PI QDs estimated from the TEM analysis and the fitting with the Brus equation (solid line). From the fitted parameters, exciton reduced mass ( $\mu$ ) and dielectric constant ( $\epsilon_r$ ) were estimated as 0.19  $m_0$  and 8.9, respectively, where  $m_0$  is electron rest mass. Considering these parameters, Bohr radius ( $R_B$ ) is calculated as ~2.5 nm using the relation:  $R_B = \frac{m_0 \epsilon_r}{\mu} (0.053) (nm)$ . The estimated values of  $\mu$ ,  $\epsilon_r$ , and  $R_B$  match fairly well with the reported values for bulk PI at RT [28,49] and it validates the use of Brus equation for strong confinement effect observed here.

To investigate the effect of temperature on luminescence and excitonic properties of perovskite QDs, temperature dependent PL spectra were acquired for F1PI and F1PB in the range of 80–300 K (see Fig. 8). Fig. 8(a) shows the temperature-dependent PL spectra of F1PI QDs. With lowering of temperature, the PL peak intensity increases monotonically and is highest at 80 K. The inset of Fig. 8(a) shows the systematic decrease in PL intensity with increasing temperature. When the temperature increases from 80 K to 300 K, we observed a systematic blue shift in PL peak position (from 739 nm to 717 nm) and significant line width broadening for F1PI. The broadening of the PL peak at higher temperature can be explained on the basis of the expansion of the unit cell of perovskite crystal that increases the crystal strain, which in turn enhances the exciton-phonon interaction resulting into peak

**Table 1**Details of sizes and the PL characteristics of the CH<sub>3</sub>NH<sub>3</sub>PbI<sub>3</sub> (PI) QDs.

Sample	QD size (nm)	Peak position (nm)	Intensity enhancement factor	PLQY (%)
F1PI	1.7	716	41	25
F2PI	3.3	721	22	13
F3PI	5.1	737	19	11
BulkPI	–	764	1	1

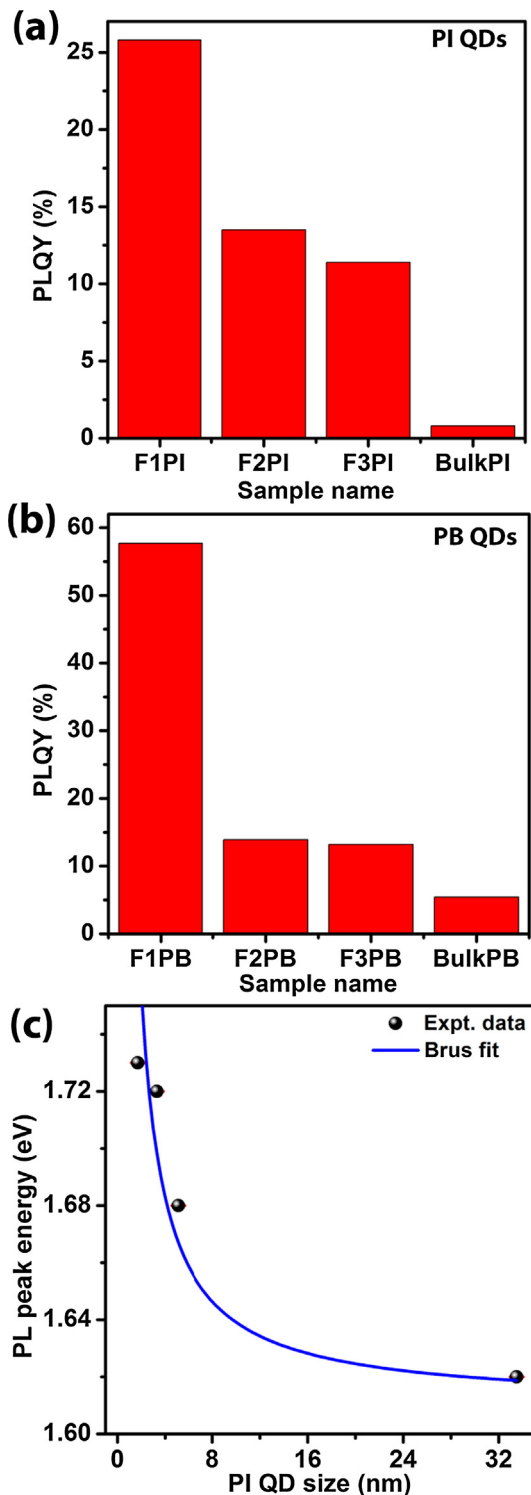


**Fig. 7.** A comparison of PLQY of various (a) PI QDs and (b) PB QDs with their bulk counterparts. (c) The spectral position of the PL peak maxima with respect to the size of PI QDs grown on the different F-TiO<sub>2</sub> templates. The points fitted to Brus equation is shown by a blue solid line. (For interpretation of the references to color in this figure legend, the reader is referred to the web version of this article.)

broadening [50]. The broadening of the PL peak at higher temperature was reported to be caused by the coupling of the excitons to acoustic phonons and to longitudinal optical (LO) phonons in GaN [51]. It has been reported that under non-resonant excitation, the enhanced carrier drift movement may result in the non-uniform redistribution of the carriers, followed by a slight broadening of

the line width of PL peak [52]. In our case, all these factors including size distribution of the QDs may be responsible for the broadening of PL peak. The electron-phonon coupling of the QDs in F1PI is studied by plotting temperature-dependent PL spectral width, as shown in Fig. 8(b). The experimental data of FWHM ( $\Gamma$ ) are fitted using Boson model given by,

$$\Gamma(T) = \Gamma_0 + \Gamma_{LO}/(\exp(\hbar\omega_{LO}/k_B T) - 1) \quad (2)$$

where  $\Gamma_0$  is the inhomogeneous broadening contribution,  $\Gamma_{LO}$  is the longitudinal exciton-optical phonon contribution to the FWHM and  $\hbar\omega_{LO}$  is the LO phonon energy. From the fitted data, the obtained parameters are as follows:  $\Gamma_0 = 57.0$  meV,  $\Gamma_{LO} = 168.3$  meV,  $\hbar\omega_{LO} = 33.8$  meV. Our result is fully consistent with reported value (25–42 meV) of optical phonon energy using Raman scattering for CH<sub>3</sub>NH<sub>3</sub>PbI<sub>3</sub> [53]. Note that no additional PL peak is observed at low-temperature regime, which discards the possibility of phase change in F1PI QDs at low temperature. Fig. 8(c) demonstrates the temperature dependence of PL peak energy of F1PI QDs. F1PI QDs exhibit a blue shift of ~57 meV in PL peak position as the temperature increases from 80 K to 300 K. The experimental data of peak energy of F1PI in the temperature range 150–290 K is fitted with the given equation [54],

$$E_g(T) = E_0 + A_{TE}T + A_{EP}(1 + 2/(\exp(\hbar\omega/k_B T) - 1)) \quad (3)$$

where  $E_0$  is the band gap at  $T = 0$  K,  $A_{TE}$  and  $A_{EP}$  are the weight of the thermal expansion (TE) and electron-phonon (EP) interaction.  $\hbar\omega$  is the optical phonon energy. From the fitted data, the values of the parameters are  $E_0 = 1.63$  eV,  $A_{TE} = 0.33$  meV/K,  $A_{EP} = 4.96$  meV and  $\hbar\omega = 42.3$  meV. These values match well with the literature [54,55]. Optical phonon energy value is comparable the value obtained from the fitting of Eq. (3). Hence, the linear increase in PL peak energy with respect to temperature may be attributed to the dominating behavior of TE while the contribution of EP is negligible in this temperature range. Fig. 8(d) shows temperature-dependent PL spectra of F1PB QDs in the range 80–300 K. Similar to the F1PI case, with increasing the temperature the PL intensity is observed to be decreased due to thermal quenching with a systematic blue shift. The phase transition induced change in PL peak (i.e. reversal of PL shift) is not observed in case of F1PB QDs [56], which discards the possibility of phase change in F1PB QDs. The room temperature (300 K) PL spectrum for F1PB shows an asymmetry in the lower energy region, indicating a trace of bound excitonic emission. The deconvoluted PL spectra of F1PB QDs at 300 K, 220 K, and 80 K are shown in Fig. S13(a–c) (Supporting Information), respectively. At 300 K, the spectral weight of peak 1 at ~525 nm appearing from free exciton recombination dominates over the bound exciton recombination (peak 2 at ~535 nm), as shown in Fig. S13(a) (Supporting Information). With lowering the temperature the bound excitonic emission increases and at 80 K, it dominates over the free excitonic recombination, as shown in Fig. S13(c) (Supporting Information). Fig. 8(e) shows the variation in PL peak energy of F1PB QDs with temperature. On the other hand, F1PB QDs show relatively weak blue shift for both the peaks (~33 meV for peak 1 and ~30 meV for peak 2) at a rate ~0.13 meV/K in the temperature range 80–300 K. This blue shift may be attributed to the electron-phonon coupling [57]. Exciton binding energy ( $E_b$ ) for the various QDs is estimated from temperature-dependent PL spectra. The temperature dependence of the integrated PL intensity of F1PB and F1PI QDs are shown in Fig. 8(f) and the experimental data are fitted using the Arrhenius equation, given by,

$$I(T) = \frac{I_0}{1 + A \exp(-E_b/k_B T)} \quad (4)$$

where  $I(T)$  and  $I_0$  are the integrated PL intensities at temperatures  $T$  and 0 K, respectively.  $A$  is a constant. In order to estimate the  $E_b$  of partially embedded perovskite QDs, the experimental data are fitted

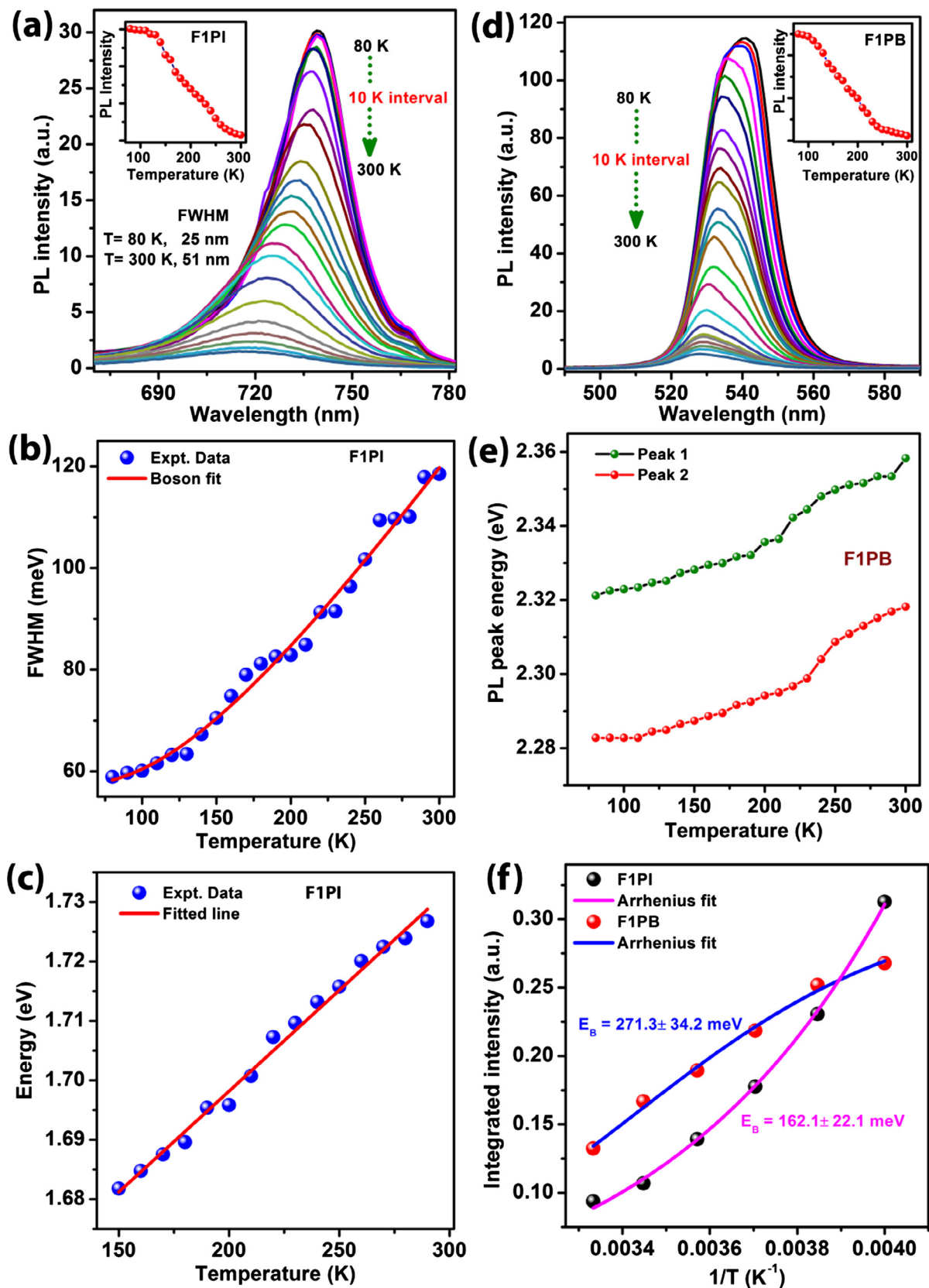


**Fig. 8.** (a) Temperature dependent PL spectra of F1PI, while the inset shows the variation of PL intensity with temperature. (b) Variation of FWHM of F1PI with temperature fitted with Boson model (Eq. (2)). The symbols represent experimental data, while the solid line corresponds to fitted data. (c) Variation of PL peak energy of F1PI with respect to temperature. The symbols represent experimental data, while the solid line corresponds to fitted data (using Eq. (3)). (d) Temperature dependent PL spectra of F1PB, while the inset shows the variation of PL intensity with temperature. (e) Variation in PL peak energy of F1PB with temperature. In the case of F1PB, two peaks (peak 1, peak 2) are fitted. (f) PL integrated intensity vs. inverse of temperature for F1PI and F1PB. The experimental data are fitted with the Arrhenius equation (Eq. (4)). The symbols represent experimental data, while the solid line corresponds to fitted data.

in the higher temperature region (250–300 K). From the fitting of the Arrhenius equation above keeping the parameters free, the  $E_b$  is estimated to be  $162.1 \pm 22.2$  meV and  $271.1 \pm 34.1$  meV for F1PI and F1PB QDs, respectively. Thus, the exciton binding energy of perovskite QDs is very high in the present case as compared to the reported values reported values for QDs as well as the bulk counterpart ( $\sim 32$  meV) [57].

Note that size dependent exciton binding energy has been reported for conventional semiconductor QDs. Using electron-hole explicitly correlated Hartree-Fock (eh-XCHF) method, it has been reported that electron-hole recombination probability and exciton binding energy for CdSe QDs follows a scaling relationship with QD size as  $d^{-n}$  and if size of the particle increases by 16.1 times, the exciton binding energy and recombination probability decreases by a factor of 12.9 and  $4.55 \times 10^5$ , respectively [58]. In our case, for the F1PI QDs, as the size decreased by  $\sim 19.4$  times (from 33 nm in bulk to 1.7 nm in QDs), the exciton binding energy increases by a factor of  $\sim 5.1$ , which is quite consistent with the above prediction, which had an error bar of 28%. For F1PB QDs, the factor comes out to be  $\sim 8.5$  times. The large increase in exciton binding energy is explained on the basis of strong confinement effect in the small QDs, where the binding energy varies as  $d^{-1}$  [51]. Thus, due to the enormous enhancement in the exciton binding energy, the perovskite QDs show stronger QC effect than their bulk counterparts. Higher exciton binding energy for perovskite QDs supports higher PLQY for QDs compared to bulk films, resulting in stable and outstandingly enhanced PL emission at room temperature [57]. Higher exciton binding energy of PB based QDs compared to the PI based QDs originates from the lower dielectric constant and larger band gap energy in F1PB [46]. Exciton binding is calculated theoretically from electron-hole interaction energy  $V_{eh}$  which is calculated from the electron-hole pair density using the expression [58],  $V_{eh} = \int d\vec{r}_e d\vec{r}_h \rho_{eh}(\vec{r}_e, \vec{r}_h) r_{eh}^{-1} \varepsilon^{-1}(\vec{r}_e, \vec{r}_h)$ , where  $\rho_{eh}$  is the electron-hole pair density function and  $\varepsilon^{-1}$  is the inverse dielectric function. Hence higher dielectric function corresponds to lower exciton binding energy. Exciton binding energy of perovskite QDs grown on F-TiO<sub>2</sub> templates is quite high compared to the other reported values for colloidal-based perovskite NP films, which makes it a very good candidate for stable light emitting and other optoelectronic applications at room temperature [59].

### 3.3.3. Time resolved photoluminescence studies

In order to investigate life time and recombination kinetics of carriers, TRPL measurement was performed on PI QDs on various F-TiO<sub>2</sub> templates and BulkPI film using a 405 nm laser excitation. The TRPL decay transients fitted with biexponential decay function can be expressed as follows:  $I(t) = \sum_{i=1}^2 A_i e^{-(t/\tau_i)}$ , where  $A_i$  is the amplitude of the TRPL decay curve corresponding to the lifetime  $\tau_i$ . The average lifetime ( $\tau_{avg}$ ) is calculated considering the following relation:  $\tau_{avg} = (A_1 \tau_1^2 + A_2 \tau_2^2) / (A_1 \tau_1 + A_2 \tau_2)$ . Fig. 9(a) shows the TRPL decay profiles of BulkPI film and various PI QDs monitoring the emission at their respective PL peak positions. The details of the individual components of BulkPI film and PI QDs are given in Table S1 (Supporting Information). The average life times are estimated to be 15.8 ns, 12.9 ns, 10.5 ns and 4.9 ns for BulkPI film, F3PI, F2PI, and F1PI, respectively. Thus, the  $\tau_{avg}$  reduces systematically with the reduction of QD size, consistent with the previous reports [14,60]. The smallest synthesized PI QDs (F1PI) possesses  $\sim 3$  fold faster recombination or short average life time compared to the BulkPI film. The shorter lifetime of PI QDs implies faster recombination and thus the higher PLQY, suggesting the PL decay of PI QDs mainly through the exciton recombination and suppression of non-radiative recombination. TRPL spectra of F1PI monitored at different emission wavelengths (660–780 nm at 20 nm intervals) are obtained under 405 nm laser excitation and the results

are shown in Fig. 9(b). Each spectrum is fitted with biexponential decay function and the fitted curve is shown by the solid line. At lower emission wavelengths, the PL decay times are observed to be shortened systematically (from 6.75 ns at 780 nm to 1.60 ns at 669 nm) confirming the QC effect of PI QDs. Thus, the broad PL spectrum for F1PI is mainly due to the variation in the PI QDs size and faster emission occurs at higher energies [43]. Since the mean decay rate ( $\Gamma$ ) is related to the PLQY by the equation:

$$PLQY = \frac{\Gamma_r}{\Gamma} = \frac{\Gamma_r}{\Gamma_{nr} + \Gamma_r} \quad (5)$$

where  $\Gamma$  is inversely proportional to  $\tau$ ,  $\Gamma_r$  and  $\Gamma_{nr}$  are the radiative and nonradiative decay rates, respectively. In our case, the PLQY of PI QDs is very high, hence the radiative recombination can be considered to be dominant over nonradiative recombination even at room temperature. Thus, the PLQY corresponding to the PI QDs may proportionally vary with  $\Gamma_r$ . The dependence of PL decay rate on the PI QDs size is plotted in Fig. 9(c). The experimental data ( $\Gamma$ ) can precisely be fitted with the relation,  $\Gamma \sim 1/d^2$ . This is fully consistent with the expected behavior that the radiative decay rate is inversely proportional to the surface area of the QDs and the number of radiative decay path increases as the QDs size decreases. For comparison, TRPL study was also performed on various PB QDs and BulkPB film with 375 nm laser excitation, as shown in Fig. S14 (a) (Supporting Information). Similar to the PI QDs,  $\tau_{avg}$  of F1PB, F2PB, F3PB, and BulkPB are found to be 3.3 ns, 7.2 ns, 9.9 ns and 20.2 ns, respectively, demonstrating the faster decay for PB QDs than the BulkPB film. PL emission corresponding to the QDs is reported to be confined in the bimolecular regime where decay rate is mainly due to radiative recombination resulting in the faster decay than the bulk film, which possesses longer decay time in the monomolecular regime due to the influence of nonradiative trap filling [61]. As the size of QD enters in the quantum regime, the confinement of electron and hole wave functions is observed to be enhanced facilitating the greater radiative transition probability, which results in the faster radiative life time [62]. TRPL spectra for F1PB recorded at different emission wavelengths (490–560 nm) at an interval of 10 nm with 375 nm laser excitation are shown in Fig. S14(b) (Supporting Information). PL decay time is observed to be shortened systematically with lowering the emission wavelength. At higher emission wavelengths, the TRPL decay profiles are observed to be overlapped, confirming the narrow size distribution of PB QDs (absence of large PB QDs), further verified by the sharp PL emission (FWHM  $\sim 24$  nm). TRPL decay profiles of cPI and cPB QDs on ITO substrates are shown in Fig. S15 (Supporting Information). The average life time of cPB and cPI QDs are  $\sim 3.8$  ns and  $\sim 27.1$  ns, respectively. Average carrier life time for F1PB and cPB QDs are nearly equal, which is consistent with their emission behavior. It reveals the fact that cPB QDs possess high radiative recombination similar to that of F1PB QDs. In contrast, the average life time of carriers in cPI QDs is larger than even the BulkPI film, which reveals the presence of nonradiative decay paths in it.

### 3.4. Photostability studies

Despite the tremendous efforts to prepare the air and photostabilized perovskites, it is still one of the major challenges for the commercialization of perovskite QD based devices. In order to test the photostability, each as-grown sample was exposed to continuous UV irradiation (360 nm laser, 18 mW at source) for several hours and PL emission was recorded at a regular interval. As shown in Fig. 9(d), the PL emission of BulkPI and BulkPB films are observed to be drastically reduced to 25% and 67% after 10 h of UV irradiation, respectively. As compared to the bulk counterpart, both the PI QDs and PB QDs show significantly improved photostability. Even after 10 h of UV irradiation, F1PB preserves  $\sim 99\%$  of its

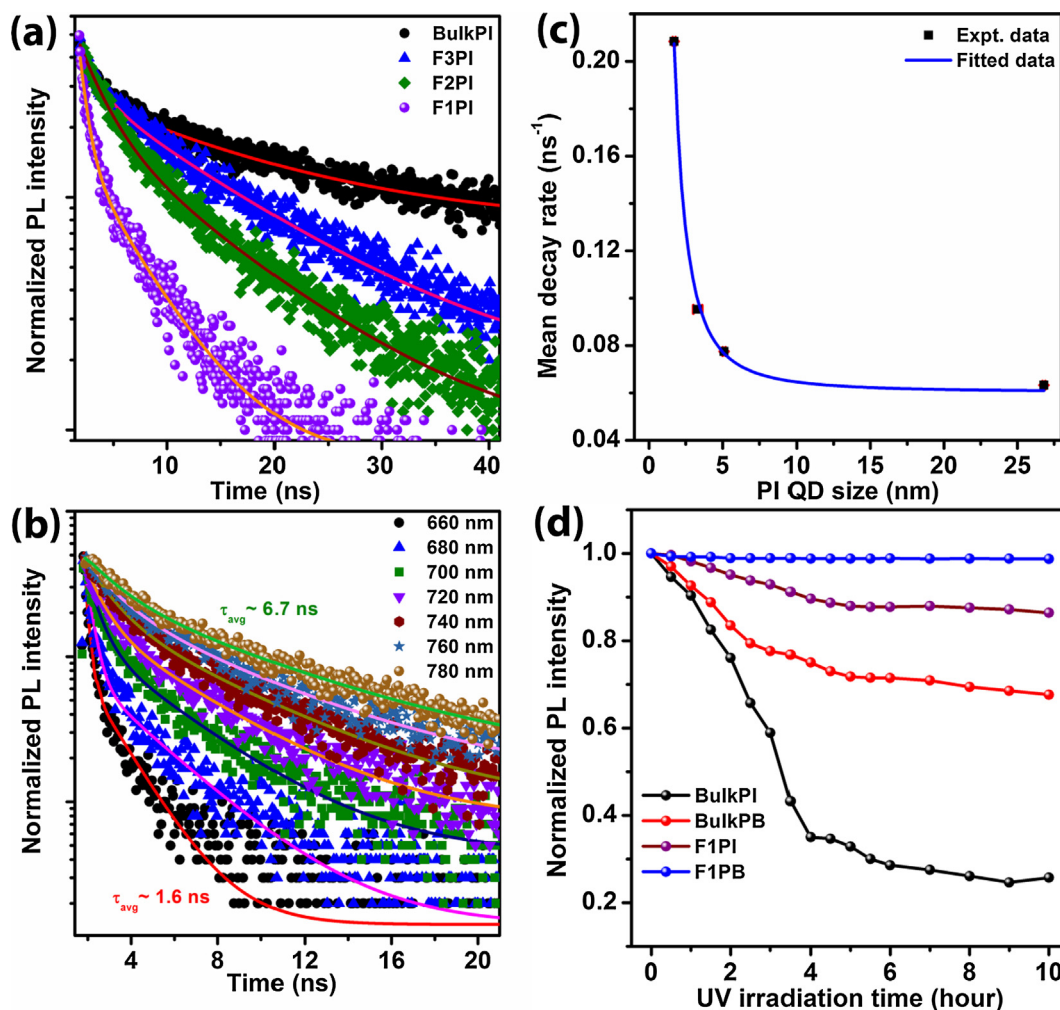


**Fig. 9.** (a) A comparison of TRPL spectra of BulkPI film, F1PI, F2PI and F3PI with 405 nm laser excitation and monitored at their respective peak position. (b) PL decay of sample F1PI monitored at different emission wavelengths. (c) PL decay rate as a function of PI QD size. Blue solid line shows the best fit curve following an inverse quadratic dependence with QD size. (d) Optical stability test of perovskite QDs (PI and PB) with 360 nm UV laser (power 18 mW at source) exposure up to 10 h. (For interpretation of the references to color in this figure legend, the reader is referred to the web version of this article.)

PL intensity, while F1PI shows ~86%. The lower stability of F1PI is due to the fact that iodide based NPs are known to be highly vulnerable to moisture and UV light. Stability of F1PI and F1PB QDs are compared with cPI and cPB QDs (see Fig. S16, Supporting Information). It's evident that cPI QDs degrade very fast under UV irradiation and PL emission reduces to ~36% of initial value after 10 h of UV irradiation. cPB QDs show better stability than the cPI QDs and it restores 90% of its initial PL intensity after 10 h of UV light exposure. Hence, perovskite QDs grown on F-TiO<sub>2</sub> template show superior stability compared to the QDs prepared using colloidal method. In the present case, the mesoporous sites of the F-TiO<sub>2</sub> flower act as the nucleation sites for the growth of perovskite QDs and these QDs are partly covered by the F-TiO<sub>2</sub> NCs, which restricts the perovskite QDs from the complete exposure to moisture and UV irradiation, preventing its fast degradation. We have observed that the as-grown perovskite QDs are quite stable in the ambient atmosphere and maintains its initial PL intensity for more than a month. For the full embedded QDs, stability is expected to be much better and would be suitable for stable device fabrication.

#### 4. Conclusion

We have reported a cost-effective and reproducible method to grow perovskite QDs partially embedded inside the pores on

F-TiO<sub>2</sub> template with high optical quality in ambient condition. Our result demonstrates that the interparticle gap between F-TiO<sub>2</sub> NCs acts as the nucleation site for the growth of crystalline perovskite QDs on a mesoporous F-TiO<sub>2</sub> template. The band gap of perovskite QDs is tuned simply by varying the pore size (void size) of the mesoporous F-TiO<sub>2</sub> templates. FESEM and TEM results reveal the uniform growth of perovskite QDs over the F-TiO<sub>2</sub> templates. Strong QC effect due to ultra-small size (~1.7 nm) of the PI and PB QDs facilitates the outstanding enhancement of PL intensity (~43 and ~124 fold, respectively) with a large spectral blue shift and these QDs exhibit very high PLQY (25% and 57%, respectively), which are significant for the template grown perovskite QDs. Quantitative analysis of the PL data reveals strong confinement effect validated by fitting the experimental data with canonical expressions derived for the quantum regime. Low-temperature PL analysis reveals ~5 and ~8.5 times higher exciton binding energy for PI QDs and PB QDs, respectively, as compared to the respective bulk films. These results are in excellent agreement with a recent theoretical prediction on size dependent exciton binding energy of QDs. The strongly enhanced PL of perovskite QDs is ascribed to enhanced radiative recombination probability and QC effect, as revealed from the TRPL analysis. The perovskite QDs grown by template-assisted method are highly stable under UV light exposure (18 mW) for >10 h, while bulk film degrades very fast. Our study offers a novel template-assisted synthesis route

for perovskite QDs with very high photo and air stability, which is promising for various optoelectronic applications including light emitting devices.

## Acknowledgments

We acknowledge the financial support from DEITY (Grant No. 5 (9)/2012-NANO (VOL-II)) for carrying out part of this work. Central Instruments Facility, I.I.T. Guwahati is acknowledged for providing the TEM and FESEM facilities.

## Appendix A. Supplementary material

Supplementary data to this article can be found online at <https://doi.org/10.1016/j.jcis.2018.12.105>.

## References

- [1] J.-P. Correa-Baena, A. Abate, M. Saliba, W. Tress, T.J. Jacobsson, M. Grätzel, A. Hagfeldt, The rapid evolution of highly efficient perovskite solar cells, *Energy Environ. Sci.* 10 (3) (2017) 710–727.
- [2] Z. Zhu, Y. Bai, X. Liu, C.C. Chueh, S. Yang, A.K.Y. Jen, Enhanced efficiency and stability of inverted perovskite solar cells using highly crystalline SnO<sub>2</sub> nanocrystals as the robust electron-transporting layer, *Adv. Mater.* 28 (30) (2016) 6478–6484.
- [3] N.-G. Park, M. Grätzel, T. Miyasaka, K. Zhu, K. Emery, Towards stable and commercially available perovskite solar cells, *Nat. Energy* 1 (11) (2016) 16152.
- [4] C.S. Ponseca Jr, T.J. Savenije, M. Abdellah, K. Zheng, A. Yartsev, T.R. Pascher, T. Harlang, P. Chabera, T. Pullerits, A. Stepanov, Organometal halide perovskite solar cell materials rationalized: ultrafast charge generation, high and microsecond-long balanced mobilities, and slow recombination, *J. Am. Chem. Soc.* 136 (14) (2014) 5189–5192.
- [5] C. Wehrenfennig, G.E. Eperon, M.B. Johnston, H.J. Snaith, L.M. Herz, High charge carrier mobilities and lifetimes in organolead trihalide perovskites, *Adv. Mater.* 26 (10) (2014) 1584–1589.
- [6] G. Xing, N. Mathews, S. Sun, S.S. Lim, Y.M. Lam, M. Grätzel, S. Mhaisalkar, T.C. Sum, Long-range balanced electron- and hole-transport lengths in organic-inorganic CH<sub>3</sub>NH<sub>3</sub>PbI<sub>3</sub>, *Science* 342 (6156) (2013) 344–347.
- [7] S.D. Stranks, G.E. Eperon, G. Grancini, C. Menelaou, M.J. Alcocer, T. Leijtens, L.M. Herz, A. Petrozza, H.J. Snaith, Electron-hole diffusion lengths exceeding 1 micrometer in an organometal trihalide perovskite absorber, *Science* 342 (6156) (2013) 341–344.
- [8] A. Kojima, K. Teshima, Y. Shirai, T. Miyasaka, Organometal halide perovskites as visible-light sensitizers for photovoltaic cells, *J. Am. Chem. Soc.* 131 (17) (2009) 6050–6051.
- [9] H.-S. Kim, C.-R. Lee, J.-H. Im, K.-B. Lee, T. Moehl, A. Marchioro, S.-J. Moon, R. Humphry-Baker, J.-H. Yum, J.E. Moser, Lead iodide perovskite sensitized all-solid-state submicron thin film mesoscopic solar cell with efficiency exceeding 9%, *Sci. Rep.* 2 (2012) 591.
- [10] W.-S. Yang, B.-W. Park, E.H. Jung, N.J. Jeon, Y.C. Kim, D.U. Lee, S.S. Shin, J. Seo, E. K. Kim, J.H. Noh, Iodide management in formamidinium-lead-halide-based perovskite layers for efficient solar cells, *Science* 356 (6345) (2017) 1376–1379.
- [11] Y. Hassan, Y. Song, R.D. Pensack, A.I. Abdelrahman, Y. Kobayashi, M.A. Winnik, G.D. Scholes, Structure-tuned lead halide perovskite nanocrystals, *Adv. Mater.* 28 (3) (2016) 566–573.
- [12] J.A. Sichert, Y. Tong, N. Mutz, M. Vollmer, S. Fischer, K.Z. Milowska, R. García Cortadella, B. Nickel, C. Cardenas-Daw, J.K. Stolarczyk, Quantum size effect in organometal halide perovskite nanoplatelets, *Nano Lett.* 15 (10) (2015) 6521–6527.
- [13] J. Cho, Y.-H. Choi, T.E. O’Loughlin, L. De Jesus, S. Banerjee, Ligand-mediated modulation of layer thicknesses of perovskite methylammonium lead bromide nanoplatelets, *Chem. Mater.* 28 (19) (2016) 6909–6916.
- [14] F. Zhang, H. Zhong, C. Chen, X.-G. Wu, X. Hu, H. Huang, J. Han, B. Zou, Y. Dong, Brightly luminescent and color-tunable colloidal CH<sub>3</sub>NH<sub>3</sub>PbX<sub>3</sub> (X = Br, I, Cl) quantum dots: potential alternatives for display technology, *ACS Nano* 9 (4) (2015) 4533–4542.
- [15] P. Tyagi, S.M. Arveson, W.A. Tisdale, Colloidal organohalide perovskite nanoplatelets exhibiting quantum confinement, *J. Phys. Chem. Lett.* 6 (10) (2015) 1911–1916.
- [16] L. Protesescu, S. Yakunin, M.I. Bodnarchuk, F. Krieg, R. Caputo, C.H. Hendon, R. X. Yang, A. Walsh, M.V. Kovalenko, Nanocrystals of cesium lead halide perovskites (CsPbX<sub>3</sub>, X = Cl, Br, and I): novel optoelectronic materials showing bright emission with wide color gamut, *Nano Lett.* 15 (6) (2015) 3692–3696.
- [17] H. Huang, F. Zhao, L. Liu, F. Zhang, X.-G. Wu, L. Shi, B. Zou, Q. Pei, H. Zhong, Emulsion synthesis of size-tunable CH<sub>3</sub>NH<sub>3</sub>PbBr<sub>3</sub> quantum dots: an alternative route toward efficient light-emitting diodes, *ACS Appl. Mater. Interface* 7 (51) (2015) 28128–28133.
- [18] V. Malgras, J. Henzie, T. Takei, Y. Yamauchi, Hybrid methylammonium lead halide perovskite nanocrystals confined in gyroidal silica templates, *ChemComm* 53 (15) (2017) 2359–2362.
- [19] S. Gonzalez-Carrero, L. Francés-Soriano, M. González-Béjar, S. Agouram, R.E. Galian, J. Pérez-Prieto, The luminescence of CH<sub>3</sub>NH<sub>3</sub>PbBr<sub>3</sub> perovskite nanoparticles crests the summit and their photostability under wet conditions is enhanced, *Small* 12 (38) (2016) 5245–5250.
- [20] L.C. Schmidt, A. Pertegás, S. González-Carrero, O. Malinkiewicz, S. Agouram, G. Mínguez Espallargas, H.J. Bolink, R.E. Galian, J. Pérez-Prieto, Nontemplate synthesis of CH<sub>3</sub>NH<sub>3</sub>PbBr<sub>3</sub> perovskite nanoparticles, *J. Am. Chem. Soc.* 136 (3) (2014) 850–853.
- [21] T. Leijtens, G.E. Eperon, N.K. Noel, S.N. Habisreutinger, A. Petrozza, H.J. Snaith, Stability of metal halide perovskite solar cells, *Adv. Energy Mater.* 5 (20) (2015).
- [22] L. Loo, P. Patel, Perovskite photovoltaics: David Mitzi addresses the promises and challenges, *MRS Bull.* 40 (8) (2015) 636.
- [23] J. Pan, S.P. Sarmah, B. Murali, I. Dursun, W. Peng, M.R. Parida, J. Liu, L. Sinatra, N. Alyami, C. Zhao, Air-stable surface-passivated perovskite quantum dots for ultra-robust, single- and two-photon-induced amplified spontaneous emission, *J. Phys. Chem. Lett.* 6 (24) (2015) 5027–5033.
- [24] S. Yang, F. Zhang, J. Tai, Y. Li, Y. Yang, H. Wang, J. Zhang, Z. Xie, B. Xu, H. Zhong, A detour strategy for colloidal stable block-copolymer grafted MAPbBr<sub>3</sub> quantum dots in water with long photoluminescence lifetime, *Nanoscale* 10 (13) (2018) 5820–5826.
- [25] A. Kojima, M. Ikegami, K. Teshima, T. Miyasaka, Highly luminescent lead bromide perovskite nanoparticles synthesized with porous alumina media, *Chem. Lett.* 41 (4) (2012) 397–399.
- [26] D. Di, K.P. Musselman, G. Li, A. Sadhanala, Y. Ievskaya, Q. Song, Z.-K. Tan, M.L. Lai, J.L. MacManus-Driscoll, N.C. Greenham, Size-dependent photon emission from organometal halide perovskite nanocrystals embedded in an organic matrix, *J. Phys. Chem. Lett.* 6 (3) (2015) 446–450.
- [27] V. Malgras, S. Tominaka, J.W. Ryan, J. Henzie, T. Takei, K. Ohara, Y. Yamauchi, Observation of quantum confinement in monodisperse methylammonium lead halide perovskite nanocrystals embedded in mesoporous silica, *J. Am. Chem. Soc.* 138 (42) (2016) 13874–13881.
- [28] M. Anaya, A. Rubino, T.C. Rojas, J.F. Galisteo-López, M.E. Calvo, H. Míguez, Strong quantum confinement and fast photoemission activation in CH<sub>3</sub>NH<sub>3</sub>PbI<sub>3</sub> perovskite nanocrystals grown within periodically mesostructured films, *Adv. Opt. Mater.* 5 (8) (2017).
- [29] S. Demchshyn, J.M. Roemer, H. Groiñ, H. Heilbrunner, C. Ulbricht, D. Apaydin, A. Böhm, U. Rütt, F. Bertram, G. Hesser, M.C. Scharber, N.S. Sariciftci, B. Nickel, S. Bauer, E.D. Glowacki, M. Kaltenbrunner, Confining metal-halide perovskites in nanoporous thin films, *Sci. Adv.* 3 (8) (2017).
- [30] J. Ghosh, R. Ghosh, P.K. Giri, Mesoporous Si nanowire templated controlled fabrication of organometal halide perovskite nanoparticles with high photoluminescence quantum yield for light-emitting applications, *ACS Appl. Nano Mater.* 1 (4) (2018) 1551–1562.
- [31] K.K. Paul, S. Jana, P. Giri, Tunable and high photoluminescence quantum yield from self-decorated TiO<sub>2</sub> quantum dots on fluorine doped mesoporous TiO<sub>2</sub> flowers by rapid thermal annealing, *Part. Part. Syst. Charact.* 1800198 (2018).
- [32] Z.-K. Tan, R.S. Moghaddam, M.L. Lai, P. Docampo, R. Higler, F. Deschler, M. Price, A. Sadhanala, L.M. Pazos, D. Credgington, F. Hanusch, T. Bein, H.J. Snaith, R.H. Friend, Bright light-emitting diodes based on organometal halide perovskite, *Nat. Nanotechnol.* 9 (2014) 687.
- [33] H. Huang, Q. Xue, B. Chen, Y. Xiong, J. Schneider, C. Zhi, H. Zhong, A.L. Rogach, Top-down fabrication of stable methylammonium lead halide perovskite nanocrystals by employing a mixture of ligands as coordinating solvents, *Angew. Chem.* 56 (32) (2017) 9571–9576.
- [34] B. Lei, V.O. Eze, T. Mori, Effect of morphology control of light absorbing layer on CH<sub>3</sub>NH<sub>3</sub>PbI<sub>3</sub> perovskite solar cells, *J. Nanosci. Nanotechnol.* 16 (4) (2016) 3176–3182.
- [35] X. Guo, C. McCleese, C. Kolodziej, A.C. Samia, Y. Zhao, C. Burda, Identification and characterization of the intermediate phase in hybrid organic-inorganic MAPbI<sub>3</sub> perovskite, *Dalton Trans.* 45 (9) (2016) 3806–3813.
- [36] Y.-H. Qiu, F. Nan, Q. Wang, X.-D. Liu, S.-J. Ding, Z.-H. Hao, L. Zhou, Q.-Q. Wang, Tuning the competitive recombination of free carriers and bound excitons in perovskite CH<sub>3</sub>NH<sub>3</sub>PbBr<sub>3</sub> single crystal, *J. Phys. Chem. C* 121 (12) (2017) 6916–6923.
- [37] K.K. Paul, P.K. Giri, Role of surface plasmons and hot electrons on the multi-step photocatalytic decay by defect enriched Ag@TiO<sub>2</sub> nanorods under visible light, *J. Phys. Chem. C* 121 (36) (2017) 20016–20030.
- [38] K.K. Paul, R. Ghosh, P.K. Giri, Mechanism of strong visible light photocatalysis by Ag<sub>2</sub>O nanoparticle-decorated monoclinic TiO<sub>2</sub> (B) porous nanorods, *Nanotechnology* 27 (31) (2016) 315703.
- [39] P. Kumar, C. Muthu, V.C. Nair, K.S. Narayan, Quantum confinement effects in organic lead tribromide perovskite nanoparticles, *J. Phys. Chem. C* 120 (32) (2016) 18333–18339.
- [40] P. Zhang, F. Yang, M.A. Kamarudin, C.H. Ng, G. Kapil, T. Ma, S. Hayase, Performance enhancement of mesoporous TiO<sub>2</sub>-based perovskite solar cells by SbI<sub>3</sub> interfacial modification layer, *ACS Appl. Mater. Interface* 10 (35) (2018) 29630–29637.
- [41] H. Seo, L.R. Baker, A. Hervier, J. Kim, J.L. Whitten, G.A. Somorjai, Generation of highly n-type titanium oxide using plasma fluorine insertion, *Nano Lett.* 11 (2) (2011) 751–756.
- [42] L.R. Baker, A. Hervier, H. Seo, G. Kennedy, K. Komvopoulos, G.A. Somorjai, Highly n-type titanium oxide as an electronically active support for platinum

- in the catalytic oxidation of carbon monoxide, *J. Phys. Chem. C* 115 (32) (2011) 16006–16011.
- [43] L. Brus, Electronic wave functions in semiconductor clusters: experiment and theory, *J. Phys. Chem.* 90 (12) (1986) 2555–2560.
- [44] K. Zheng, Q. Zhu, M. Abdellah, M.E. Messing, W. Zhang, A. Generalov, Y. Niu, L. Ribaud, S.E. Canton, T.N. Pullerits, Exciton binding energy and the nature of emissive states in organometal halide perovskites, *J. Phys. Chem. Lett.* 6 (15) (2015) 2969–2975.
- [45] Y.H. Kim, H. Cho, J.H. Heo, T.S. Kim, N. Myoung, C.L. Lee, S.H. Im, T.W. Lee, Multicolored organic/inorganic hybrid perovskite light-emitting diodes, *Adv. Mater.* 27 (7) (2015) 1248–1254.
- [46] K. Tanaka, T. Takahashi, T. Ban, T. Kondo, K. Uchida, N. Miura, Comparative study on the excitons in lead-halide-based perovskite-type crystals  $\text{CH}_3\text{NH}_3\text{PbBr}_3$ ,  $\text{CH}_3\text{NH}_3\text{PbI}_3$ , *Solid State Commun.* 127 (9) (2003) 619–623.
- [47] M. Hirasawa, T. Ishihara, T. Goto, K. Uchida, N. Miura, Magnetoabsorption of the lowest exciton in perovskite-type compound  $(\text{CH}_3\text{NH}_3)_2\text{PbI}_4$ , *Phys. B Condens. Matter.* 201 (1994) 427–430.
- [48] A. Buin, R. Comin, A.H. Ip, E.H. Sargent, Perovskite quantum dots modeled using ab initio and replica exchange molecular dynamics, *J. Phys. Chem. C* 119 (24) (2015) 13965–13971.
- [49] V. D’Innocenzo, G. Grancini, M.J.P. Alcocer, A.R.S. Kandada, S.D. Stranks, M.M. Lee, G. Lanzani, H.J. Snaith, A. Petrozza, Excitons versus free charges in organolead tri-halide perovskites, *Nat. Commun.* 5 (2014) 3586.
- [50] S. Zhuang, D. Xu, J. Xu, B. Wu, Y. Zhang, X. Dong, G. Li, B. Zhang, G. Du, Temperature-dependent photoluminescence on organic inorganic metal halide perovskite  $\text{CH}_3\text{NH}_3\text{PbI}_{3-x}\text{Cl}_x$  prepared on ZnO/FTO substrates using a two-step method, *Chin. Phys. B* 26 (1) (2017) 017802.
- [51] G. Franssen, E. Litwin-Staszewska, R. Piotrkowski, T. Suski, P. Perlin, Optical and electrical properties of homoepitaxially grown multiquantum well InGaN/GaN light-emitting diodes, *J. Appl. Phys.* 94 (9) (2003) 6122–6128.
- [52] T. Lu, Z. Ma, C. Du, Y. Fang, H. Wu, Y. Jiang, L. Wang, L. Dai, H. Jia, W. Liu, H. Chen, Temperature-dependent photoluminescence in light-emitting diodes, *Sci. Rep.* 4 (2014) 6131.
- [53] C. Quarti, G. Grancini, E. Mosconi, P. Bruno, J.M. Ball, M.M. Lee, H.J. Snaith, A. Petrozza, F. De Angelis, The Raman spectrum of the  $\text{CH}_3\text{NH}_3\text{PbI}_3$  hybrid perovskite: interplay of theory and experiment, *J. Phys. Chem. Lett.* 5 (2) (2013) 279–284.
- [54] K. Wei, Z. Xu, R. Chen, X. Zheng, X. Cheng, T. Jiang, Temperature-dependent excitonic photoluminescence excited by two-photon absorption in perovskite  $\text{CsPbBr}_3$  quantum dots, *Opt. Lett.* 41 (16) (2016) 3821–3824.
- [55] B. Ai, C. Liu, Z. Deng, J. Wang, J. Han, X. Zhao, Low temperature photoluminescence properties of  $\text{CsPbBr}_3$  quantum dots embedded in glasses, *Phys. Chem. Chem. Phys.* 19 (26) (2017) 17349–17355.
- [56] J. Dai, H. Zheng, C. Zhu, J. Lu, C. Xu, Comparative investigation on temperature-dependent photoluminescence of  $\text{CH}_3\text{NH}_3\text{PbBr}_3$  and  $\text{CH}(\text{NH}_2)_2\text{PbBr}_3$  microstructures, *J. Mater. Chem. C* 4 (20) (2016) 4408–4413.
- [57] J. Li, X. Yuan, P. Jing, J. Li, M. Wei, J. Hua, J. Zhao, L. Tian, Temperature-dependent photoluminescence of inorganic perovskite nanocrystal films, *RSC Adv.* 6 (82) (2016) 78311–78316.
- [58] J.M. Elward, A. Chakraborty, Effect of dot size on exciton binding energy and electron-hole recombination probability in CdSe quantum dots, *J. Chem. Theory Comput.* 9 (10) (2013) 4351–4359.
- [59] K. Wu, A. Bera, C. Ma, Y. Du, Y. Yang, L. Li, T. Wu, Temperature-dependent excitonic photoluminescence of hybrid organometal halide perovskite films, *Phys. Chem. Chem. Phys.* 16 (41) (2014) 22476–22481.
- [60] M. Zhang, H. Yu, M. Lyu, Q. Wang, J.-H. Yun, L. Wang, Composition-dependent photoluminescence intensity and prolonged recombination lifetime of perovskite  $\text{CH}_3\text{NH}_3\text{PbBr}_{3-x}\text{Cl}_x$  films, *Chem. Commun.* 50 (79) (2014) 11727–11730.
- [61] S.D. Stranks, V.M. Burlakov, T. Leijtens, J.M. Ball, A. Goriely, H.J. Snaith, Recombination kinetics in organic-inorganic perovskites: excitons, free charge, and subgap states, *Phys. Rev. Appl.* 2 (3) (2014) 034007.
- [62] V.K. Ravi, A. Swarnkar, R. Chakraborty, A. Nag, Excellent green but less impressive blue luminescence from  $\text{CsPbBr}_3$  perovskite nanocubes and nanoplatelets, *Nanotechnology* 27 (32) (2016) 325708.